A Revised Land Surface Parameterization (SiB2) for Atmospheric GCMs. Part II: The Generation of Global Fields of Terrestrial Biophysical Parameters from Satellite Data

PIERS J. SELLERS,* SIETSE O. LOS,† COMPTON J. TUCKER,* CHRISTOPHER O. JUSTICE,@ DONALD A. DAZLICH,# G. JAMES COLLATZ,* AND DAVID A. RANDALL#

*NASA/GSFC, Greenbelt Maryland
†Science Systems and Applications Inc., NASA/GSFC, Greenbelt, Maryland
@Laboratory for Global Remote Sensing, Lefrak Hall, University of Maryland, College Park, Maryland
#Department of Atmospheric Sciences, Colorado State University, Fort Collins, Colorado

(Manuscript received 23 June 1994, in final form 1 August 1995)

ABSTRACT

The global parameter fields used in the revised Simple Biosphere Model (SiB2) of Sellers et al. are reviewed. The most important innovation over the earlier SiB1 parameter set of Dorman and Sellers is the use of satellite data to specify the time-varying phenological properties of FPAR, leaf area index, and canopy greenness fraction. This was done by processing a monthly 1° by 1° normalized difference vegetation index (NDVI) dataset obtained from Advanced Very High Resolution Radiometer red and near-infrared data. Corrections were applied to the source NDVI dataset to account for (i) obvious anomalies in the data time series, (ii) the effect of variations in solar zenith angle, (iii) data dropouts in cold regions where a temperature threshold procedure designed to screen for clouds also eliminated cold land surface points, and (iv) persistent cloud cover in the Tropics. An outline of the procedures for calculating the land surface parameters from the corrected NDVI dataset is given, and a brief description is provided of source material, mainly derived from in situ observations, that was used in addition to the NDVI data. The datasets summarized in this paper should be superior to prescriptions currently used in most land surface parameterizations in that the spatial and temporal dynamics of key land surface parameters, in particular those related to vegetation, are obtained directly from a consistent set of global-scale observations instead of being inferred from a variety of survey-based land-cover classifications.

1. Introduction

The last decade has seen significant progress in the development of land surface parameterizations (LSPs) for use within general circulation models of the atmosphere (GCMs). Dickinson (1984) and Sellers et al. (1986) designed and implemented LSPs based on biophysical principles and showed that their implementation in GCMs resulted in improved simulation of the continental fields of absorbed radiation, evapotranspiration, and precipitation (Sato et al. 1989).

The first generation of biophysical LSPs, BATS of Dickinson (1984), and the Simple Biosphere model (SiB) of Sellers et al. (1986) were designed to provide improved estimates of the exchanges of radiation, moisture, sensible heat, and momentum between the land surface and the atmosphere. The important parameters governing these exchanges are the albedo (radiative transfer), the roughness length (momentum transfer and turbulent exchange of heat and moisture), and the surface resistance (control of moisture flux from the vegetation and soil to the air). The surface resistance replaces the moisture availability functions used in earlier LSPs (see, for example, Budyko 1974). All GCMs require specification of these parameters or related quantities as time series global fields. Until the mid 1980s these were arbitrarily prescribed as independent boundary conditions or by using numbers inferred from field measurements. Dickinson (1983, 1984) and Sellers et al. (1986) developed submodels for LSPs that calculated these parameters from knowledge of a few vegetation and soil quantities that could be directly measured or attributed to specific vegetation types (Table 1). To obtain global fields for these parameters, the world's land-cover types as defined by Kuchler (1983) and Matthews (1984) were lumped into 12 classes (Table 2), each of which was assigned values for the quantities listed in Table 1 based on an extensive survey of the ecological literature (Klink and Willmott 1985). The global distribution of land surface parameters was obtained by combining Table 1 with Table 2. This was a difficult and inexact task in the case of the phenological parameters of leaf area index and canopy greenness fraction, which are essential for calculating the desired parameters. Dorman and Sellers (1989) used this approach for the original version of SiB (hereafter referred to as

Corresponding author address: Dr. Piers J. Sellers, Biospheric Sciences Branch/NASA/GSFC, Code 923, Greenbelt, MD 20771.

TABLE 1. Summary of parameters used by SiB1 and SiB2 submodels. Note how some parameters are common to more than one submodel, ensuring consistency among the derived fields of albedo, roughness, and energy fluxes. Time-varying parameters are denoted by asterisk. (Note that N is used to define daily mean leaf optical properties by weighting "live" and "dead" values held in the input parameter set.) The same parameter categories apply to SiB2, except that only root depth is assigned for the category "root physiology, morphology." In SiB1 and SiB2, total leaf area index L_T and the canopy greenness fraction N vary seasonally. In SiB1, all vegetation of the same class in the same hemisphere has the same phenology, except for wheat where a simple latitudinal dependence is included (see Dorman and Sellers 1989). In SiB2, L_T and N are defined by vegetation type and satellite data and therefore vary temporally and spatially within vegetation classes.

	Radiative transfer	Momentum transfer	Stomatal resistance
* Leaf area index, L_T	X	X	X
* Canopy greenness fraction, N	X		X
Leaf-angle distribution function, $G(\mu)$	X	X	X
Cover fraction, V	X	X	X
Leaf optical properties	X		X
Soil optical properties	X		
Canopy-top and -base heights		X	
Leaf dimension		X	
Leaf physiological properties			X
Root physiology, morphology			X
Soil physical properties			X

SiB1) to calculate a global climatology of albedo, roughness length, and stomatal resistance.

SiB1 has since been modified to include a more realistic model of leaf photosynthesis and conductance as proposed by Collatz et al. (1991, 1992). This leaf-scale model was analytically integrated to describe canopy conductance and photosynthesis as a function of physiological properties (specified for each vegetation type as in Table 1), environmental conditions (provided by the GCM), and the canopy photosynthetically active radiation (PAR) use parameter, Π, which is defined as the fraction of photosynthetically active radiation absorbed by the green canopy (FPAR) divided by the mean canopy PAR extinction coefficient, $\bar{k}$: $\Pi = \text{FPAR}/\bar{k}$ (Sellers et al. 1992a, 1996). SiB2 requires definition of global time-varying fields of FPAR, total leaf area index L_T, and canopy greenness fraction N, which are of course closely related, to calculate the carbon assimilation rate or gross photosynthesis in addition to the fluxes of radiation, heat, moisture, and momentum. This task could be carried out using the methods described in Dorman and Sellers (1989). However, it is difficult to place much confidence in the accuracy of these survey-derived fields because of the large variations in the spatial and temporal patterns of FPAR, L_T, and canopy greenness fraction N within land-cover classes. To do better, we must make use of satellite data, which alone can provide us with a continuous, consistent, global view of the world's vegetation.

This paper outlines a procedure for calculating global monthly fields of FPAR from the satellite-derived normalized difference vegetation index (NDVI) dataset by Los et al. (1994). A number of steps are involved in moving from the source NDVI dataset to FPAR and then to the required values of albedo (obtained from spectral hemispheric reflectances, $a_{\Lambda,\mu}$), roughness length z_0, and canopy conductance g_c. A summary is as follows:

(i) Simple corrections were applied to the 1° by 1° source NDVI data to account for anomalies in the seasonal time series, solar zenith angle effects, data dropouts, and persistent cloud cover. The resulting product is called FASIR-NDVI and is described in detail in sections 3 and 4.

(ii) The FASIR-NDVI fields were combined with a land-cover classification to derive fields of FPAR. These were analyzed in turn to calculate total leaf area index L_T and canopy greenness fraction N (see section 5).

(iii) The fields of L_T and N were used to calculate hemispheric surface reflectances $a_{\Lambda,\mu}$ and roughness lengths z_0 using simple models (see section 6). FPAR itself is used directly in SiB2 to calculate canopy photosynthesis A_c and conductance g_c, and hence the surface energy balance [see section 6 and Sellers et al. (1992a)].

The satellite data are thus used to specify monthly values of FPAR, leaf area index, and canopy greenness fraction for each 1° by 1° grid area. Additional vegetation and soil parameters are required to further interpret these quantities into higher-order parameters (albedo, roughness length, canopy conductance) and also for direct use in the LSP-GCM. These nonsatellite-derived parameters are specified from literature sources in much the same way as was done in Dorman and Sellers (1989).

A companion paper by Sellers et al. (1996) describes the formulation of SiB2 in full. Another companion paper by Randall et al. (1996) describes the performance of SiB2 within a GCM.

2. Theoretical background

The complete formulation of SiB2 is set out in Sellers et al. (1996) and papers referenced from it. For the purpose of illustration, a brief summary of the governing equations is presented below in order to show the role of the principal surface parameters in the energy and heat balance.

The total surface energy balance is given by

$$R_n - G = \lambda E + H, \quad (1)$$

where

R_n = net radiation (W m^{-2})
G = ground heat flux (W m^{-2})
λE = latent heat flux (W m^{-2})
H = sensible heat flux (W m^{-2}).

a. Albedo

The net radiation, R_n, is given by

$$R_n = \int_0^{4.0\ \mu m} \int_0^{\pi/2} F_{\Lambda,\mu}\downarrow (1 - a_{\Lambda,\mu}) d\mu d\Lambda + \epsilon(F_{T,d}\downarrow - \sigma T_s^4), \quad (2)$$

where

$F_{\Lambda,\mu}\downarrow$ = incoming radiation flux (W m^{-2});
Λ = (subscript) wavelength interval (μm);
μ = (subscript) cosine of angle of incident radiation;
$a_{\Lambda,\mu}$ = surface hemispheric reflectance;
ϵ = emissivity $\approx$ 1.0;
$F_{T,d}\downarrow$ = incident thermal infrared radiation (TIR) (assumed to be all diffuse) (W m^{-2});
T = (subscript) thermal wavelength interval;
d = (subscript) diffuse radiation;
σ = Stefan–Boltzman constant (W m^{-2} K^{-1});
T_s = surface temperature (K).

In SiB2, the vegetation cover is "bulked" into a single layer overlying the soil rather than two layers as used in SiB1. A two-stream approximation model is used to calculate hemispherical surface reflectances for incident direct and diffuse visible and near-infrared (NIR) radiation (Sellers 1985). The functions of Λ, μ in (2) are therefore divided into four reflectances (visible direct, visible diffuse, NIR direct and NIR diffuse), with the spectral division between visible and NIR wavebands specified at 0.7 μm, which corresponds to the abrupt change in leaf and chlorophyll optical properties. Dorman and Sellers (1989) presented evidence that the calculation of surface reflectances by this method gave results that compare well with field observations in areas of moderate to dense vegetation cover. In semiarid and desert areas, the results were not so good because a single set of soil background reflectances was assigned to all arid areas in the world: this is unrealistic (Harrison et al. 1990).

Generally speaking, absolute errors or uncertainties in the albedo translate almost directly into errors in the calculation of net radiation and the heat fluxes of (1). This is because the surface net shortwave flux is around five times as large, although of opposite sign, as the net longwave flux (Sato et al. 1989; Table 1).

The calculated reflectances and albedo of (2) are functions of the surface radiative transfer properties specified in Table 1. Of these properties, the leaf spectral characteristics (live and dead) and the leaf-angle distribution function can be assigned using published values; within vegetation classes, these parameters do not vary widely temporally or spatially, except when the vegetation is senescent. Soil reflectance usually plays a lesser role in the albedo of vegetated areas, but in arid areas it must be specified from direct observations. The major uncertainty in determining albedo by this method is therefore related to the amount and greenness of the vegetation cover.

Sellers (1987) explored the dependence of canopy reflectance on leaf area index and spectral properties using the two-stream model. It was shown that for a continuous canopy of horizontal leaves, for a specified wavelength interval,

$$a = \frac{\omega}{2}\left(\frac{1 - A}{P_1 - P_2 A}\right), \quad (3)$$

where

a = surface reflectance;
$A = [(P_1 - \gamma)/(P_2 - \gamma)]e^{-2h_a L_T}$;
ω = leaf scattering coefficient;
$P_1 = 1 - \omega/2 + h_a$;
$P_2 = 1 - \omega/2 - h_a$;
$h_a = (1 - \omega)^{1/2}$, extinction coefficient for diffuse radiation;
$\gamma = \omega/2a_s$;
a_s = soil reflectance.

Similar expressions were derived for spherical and other leaf-angle distributions. In (3), we see that reflectance depends strongly on the $e^{-2h_a L_T}$ term, where $2h_a$ is around 1.8 for visible radiation and 0.5 for NIR. In practice, most soil reflectances in vegetated areas are fairly dark so the total albedo is weakly dependent on variations in the visible reflectance and more strongly dependent on the NIR contribution (Fig. 1). Clearly, arid zones with bright soil backgrounds are the exception to this generalization, but the numerical consequences of applying this assumption do not seem to be serious (see later discussion, section 7).

b. Surface roughness

Turbulent exchange between the surface and the atmosphere determines not only the local-scale transfer of momentum, but also the transport of sensible and latent heat away from the surface. The details of the SiB2 aerodynamic transfer model are written up in Sellers et al. (1996). Here we summarize the relation-

TABLE 2. SiB2 vegetation classification derived from the Matthews (1983, 1984, 1985) and Kuchler (1983) land-cover datasets. The new SiB2 vegetation assignments (in column headed "land-cover type") used at the 4° by 5° resolution are shown together with the original SiB class identifiers (1 through 12; between brackets in column headed "land-cover type") used at the 1° by 1° resolution. Note that as SiB2 has only one vegetation layer, there are no longer any two-layer classes (e.g., tree–grass savanna) as in SiB1. The actual number of land-cover classes in SiB2 is now only nine since types 6, 7, 8, and 11 are now all assigned C_4 grassland properties. The abbreviations in the "Kuchler" and "Matthews" columns refer to the 32 classes identified in the original datasets. No one-to-one agreement between the 32 Kuchler and Matthews classes is implied. The reconstruction procedure for broadleaf evergreen vegetation types (see section 4d) was not applied to class 9 of the original Matthews classification (between brackets in column headed "Matthews").

Land-cover type	Kuchler	Matthews	N (1° × 1°)	Area (10^6 km^2)	SiB1	SiB2
Tall vegetation						
Broadleaf-evergreen trees	B	1	1433	17.2	1	1
	S	2				
		3				
		(9)				
Broadleaf-deciduous trees	D	5	258	2.2	2	2
	Di					
	DBs					
Broadleaf and needleleaf trees	M	10	487	3.9	3	3
	ND					
	SE					
Needleleaf-evergreen trees	E	4	2156	14.8	4	4
	Ep	7				
		8				
		14				
Needleleaf-deciduous trees	N	16	1117	6.1	5	5
		11				
Short vegetation						
C_4 groundcover	DG	13	4316	46.4	6	6
(+ tall vegetation)	GBp	15				
	GD	23				
	DGp	24				
	Gsp					
(grassland)	G	25			7	6
	Gp	26				
		27				
		28				
		29				
(shrubs + groundcover)	Bs	6			8	6
	Bz, Bzi	12				
	Ds					
	Dsi, Bzi					
	DsG					
	GDsp					
	Ss					
	SsG					
	Szp					
(bare soil)	b	30			11	6
Shrubs with bare soil	Bsp	17	911	9.4	9	7
	Dsp	19				
	Dzp	21				
Dwarf trees and shrubs	L	18	1252	5.9	10	8
		20				
		22				
Agriculture or C_3 grassland	n/a	32	2783	26.2	12	9
Total			22097	147.8		

ships between shear stress, aerodynamic resistance, and roughness length. Under neutral conditions

$$\tau = \rho \frac{u_m}{r_a}, \tag{4}$$

where

τ = shear stress (kg m^{-1} s^{-2});
ρ = air density (kg m^{-3});
u_m = wind speed at reference height (m s^{-1});
r_a = aerodynamic resistance for momentum transfer (s m^{-1}).

Also,

$$r_a = \frac{1}{u_m}\left(\frac{1}{k}\log\frac{z_m - d}{z_0}\right)^2, \tag{5}$$

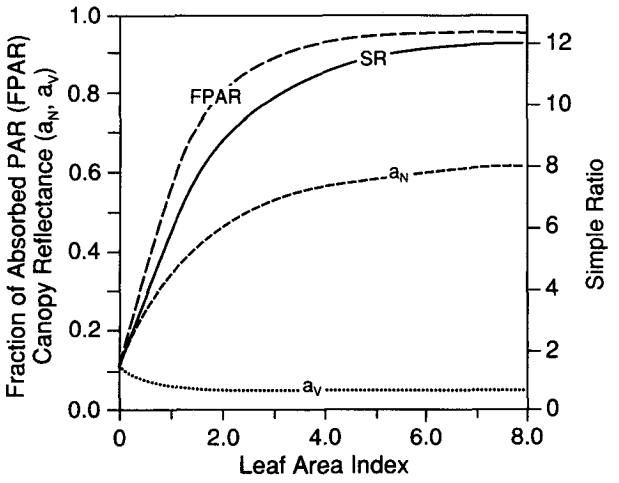

FIG. 1. Variation of visible (V) and NIR (N) reflectance, simple ratio (SR), and fraction of photosynthetically active radiation absorbed by the green part of vegetation (FPAR), with leaf area index. (Green canopy, horizontal leaves; from Sellers et al. 1992a.)

where

k = von Kármán's constant (≈0.41);
z_m = reference height (m);
d = zero plane displacement (m);
z_0 = roughness length (m).

In (4) and (5) we see that τ and r_a are related to the natural logarithm of z_0. The SiB turbulent transfer submodel calculates values of z_0 and d from the list of parameters shown in Tables 1 and 6 and yields a very weak exponential dependence on leaf area index (Fig. 2). Over the normal range of leaf area index, that is, $0.5 < L_T < 5.0$, a simple expression can be plotted to the results of Sellers et al. (1989) to yield

$$z_0 = z_2(1 - b_z e^{-h_z L_T}), \tag{6}$$

where

z_2 = canopy height (m);
$b_z \approx 0.91$;
$h_z \approx 0.0075$.

c. *Photosynthesis and evapotranspiration*

The details of the formulation used to calculate coupled photosynthesis and transpiration are presented in Sellers et al. (1992a, 1996). The model calculates canopy photosynthesis and conductance as the product of three terms:

$$A_c = (V_{\max_0}, F_{\pi_0}\downarrow)(B_1 \cdots B_4)(\Pi) \tag{7a}$$

$$g_c = (V_{\max_0}, F_{\pi_0}\downarrow)(B_1 \cdots B_6)(\Pi), \tag{7b}$$

where

A_c = canopy photosynthetic rate (mol m^{-2} s^{-1});
g_c = canopy conductance (m s^{-1});
$V_{\max_0}$ = maximum leaf catalytic (Rubisco) capacity for green sun leaves (mol m^{-2} s^{-1});
$F_{\pi_0}\downarrow$ = incident radiant flux of photosynthetically active (visible, 0.4–0.7 μm) radiation (W m^{-2});
$B_1 \cdots B_6$ = environmental stress factors dependent on temperature, relative humidity and soil moisture;
Π = canopy PAR use parameter.

The first two terms of (7) are dependent on the vegetation physiology ($V_{\max_0}$), the incident flux of PAR (F_{π_0}), and local environmental conditions ($B_1 \ldots B_6$) (see Sellers et al. 1992a, 1996). The vegetation physiological parameters and the coefficients governing B_1 and B_6 have been assigned from published values (see Table 5 and Sellers et al. 1996). The crucial surface parameter in (7) is the canopy PAR-use parameter Π, which specifies the amount of green vegetation present; it varies from 0 (no vegetation) to around 1.5 (dense, green vegetation) (Sellers et al. 1992a):

$$\Pi \approx \frac{\text{FPAR}}{\bar{k}}, \tag{8}$$

where

FPAR = fraction of PAR absorbed by the green vegetation canopy;
$\bar{k}$ = time–mean (radiation-weighted) extinction coefficient for PAR.

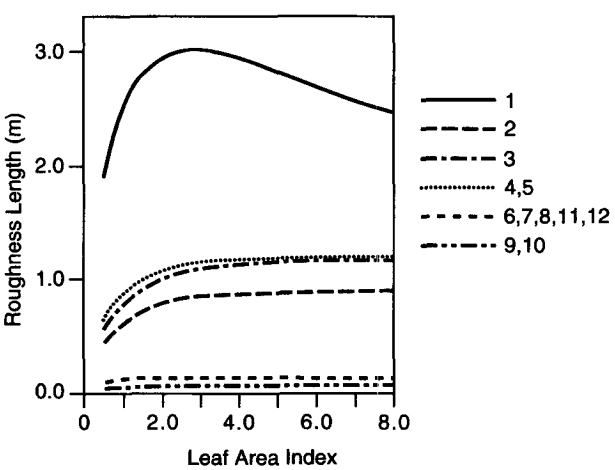

FIG. 2. Dependence of roughness length z_0 on total leaf area index, L_T, as calculated by the turbulent transfer submodel of SiB (from Sellers et al. 1989, 1996). The numbers in the legend correspond to the numbers of the biome types in Table 2.

FPAR can be approximated by

$$\text{FPAR} = VN(1 - e^{-\bar{k}L_T/V}), \tag{9}$$

where

V = vegetation-cover fraction;
N = canopy greenness fraction [(26)];
L_T = total leaf area index.

The conductance g_c given by (7b) is used to calculate the canopy transpiration rate in SiB2. For a dry canopy with negligible energy fluxes to or from the soil, the SiB2 formulation approaches the Penman–Monteith equation

$$\lambda E = \frac{\Delta(R_n - G) + \rho c_p \delta_e / r_a}{\Delta + \gamma(r_c + r_a)/r_a}, \tag{10}$$

where

Δ = slope of the saturated vapor pressure versus temperature curve (Pa K^{-1});
γ = psychrometric constant (Pa K^{-1});
δ_e = vapor pressure deficit at z_m (Pa) $= e^*(T_m) - e_m$
T_m; e_m = air temperature (K); vapor pressure at z_m (Pa);
$e^*(T_m)$ = saturated vapor pressure at temperature T_m (Pa);
r_a = aerodynamic resistance for heat and water vapor (s m^{-1});
r_c = canopy resistance (s m^{-1}) $(=1/g_c)$.

In (10) the aerodynamic resistance for heat and water vapor r_a is closely related to r_a for momentum in (4); the value of z_0 for heat and water vapor transport is smaller than that for momentum (Sellers et al. 1986).

Under normal daytime conditions, the numerator of (10)—the evaporative demand—holds a moderate or high value. The evaporation rate is then largely regulated by the surface resistance, r_c, which is typically five or more times as large as r_a for most natural vegetation covers (Fig. 3) (Sato et al. 1989; Sellers et al. 1992b).

d. Deriving surface parameters from satellite data

Equations (2), (4), (7), and (10) define the fluxes of radiation (albedo), momentum (roughness length), photosynthesis, and evapotranspiration (biophysical control of gas exchange and surface heat fluxes), respectively. It should be noted that the governing parameters a, z_0, and FPAR are not linearly related to total leaf-area index, but to its exponent, such that

albedo, a, varies approximately with $e^{-2h_aL_T/V}$, V, N
z_0 varies approximately with $e^{-h_zL_T/V}$, V
FPAR varies approximately with $e^{-\bar{k}L_T/V}$, V, N

where h_a, h_z, and $\bar{k}$ are extinction coefficients and N is the canopy greenness fraction. The extinction coefficients $2h_a$ and k vary around 0.5 for green vegetation (h_z is small and for practical purposes z_0 is dependent on vegetation height to first order and only weakly on leaf area index). Thus, we see that the transfers of radiation and mass (H_2O and CO_2) are sensitive to leaf area index at low values of L_T but can be expected to asymptote with increasing L_T.

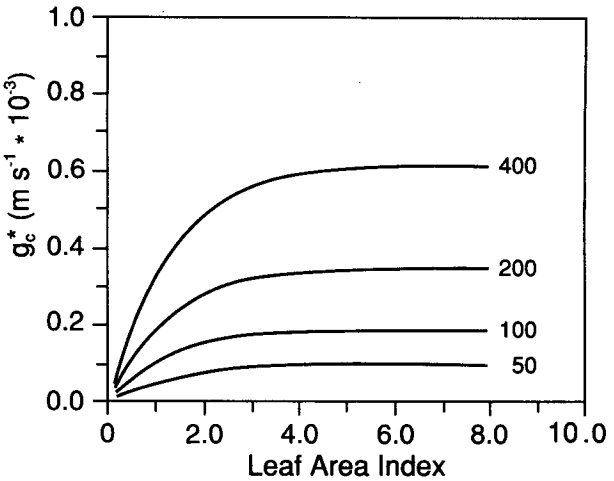

FIG. 3. Dependence of unstressed surface conductance ($g_c^* = 1/r_c^*$) on green leaf area index, L_g (from Sellers et al. 1992a).

Sellers et al. (1992a) built on work by Dickinson (1983), Asrar et al. (1984), Sellers (1985, 1987), Hall et al. (1990), and Myneni et al. (1992) on remote sensing of vegetation, and on work by Farquhar et al. (1980), Ball (1988), and Collatz et al. (1991) on plant physiology, to derive the relations between photosynthesis, conductance, and FPAR shown in (7), and also between FPAR and satellite-derived surface reflectances discussed below.

Two remotely sensed vegetation indices are in common use, defined here as

$$\text{SR} = \frac{a_N}{a_V}$$

$$\text{NDVI} = \frac{a_N - a_V}{a_N + a_V}, \tag{11}$$

where

SR = simple ratio;
NDVI = normalized difference vegetation index;
a_V, a_N = hemispheric reflectances, or radiances, for visible and NIR wavelength intervals, respectively (sensor dependent).

In the theoretical treatment of Sellers et al. (1992a), a_V and a_N are taken as above-canopy reflectances, that is, the effects of atmospheric absorption and scattering were ignored. In this paper, a_V and a_N are replaced by radiances normalized for incoming solar radiation as observed by a satellite sensor.

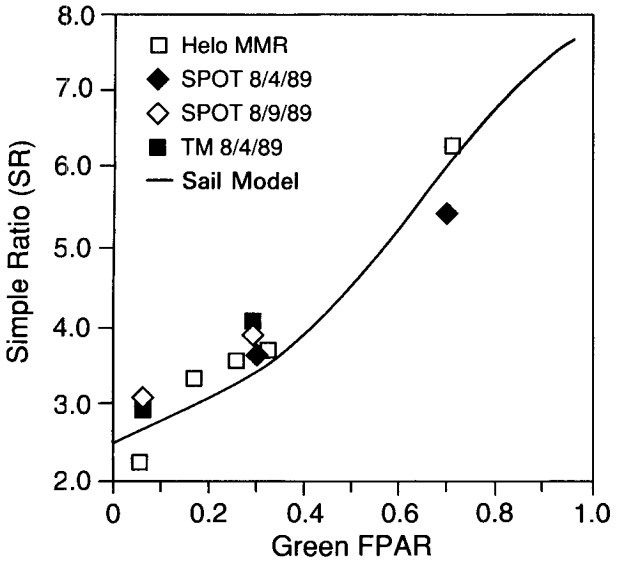

FIG. 4. Relationship between simple ratio vegetation index (SR) and FPAR for the FIFE study area (redrawn from Hall et al. 1992). The SR data were taken from atmospherically corrected satellite and helicopter data. The FPAR data were made from light bar observations (green FPAR only). The line is a simulation produced by the SAIL model (Hall et al. 1992).

Sellers (1987) used a two-stream model to show that for idealized conditions—uniform green canopy, dark underlying surface—the spectral vegetation indices should be proportional to the NIR reflectance a_N and to FPAR. It was shown that this useful relationship holds because the broadband leaf-scattering coefficients in the visible ($\omega_V \approx 0.2$) and the NIR ($\omega_N \approx 0.95$) are such that

$$\frac{\partial a_N}{\partial L_T} \propto \frac{\partial \text{FPAR}}{\partial L_T} \quad \text{for all values of } L_T. \tag{12}$$

Equation (12) holds because the extinction coefficient for PAR flux or visible radiation (k) is roughly double the extinction coefficient for diffuse NIR flux (h_N) within the canopy, or

$$k \approx 2h_N, \tag{13a}$$

which may be reexpressed as

$$\frac{G(\mu)}{\mu}(1 - \omega_V)^{1/2} = 2(1 - \omega_N)^{1/2}, \tag{13b}$$

where

$G(\mu)$ = relative projected area of leaves in direction $\cos^{-1}\mu$,
μ = cosine of solar zenith angle.

Simply put, (12) and (13) hold because the near-infrared reflectance a_N, which drives the SR and NDVI under most conditions, is proportional to double the pathlength of NIR radiation in the canopy ($e^{-2h_N L_T/V}$) since this radiation must enter, interact, and leave the canopy, while FPAR is proportional to only the one-way penetration and absorption of PAR through the canopy ($e^{-kL_T/V}$). The two parameters, a_N and FPAR, vary with each other if (13) is approximately satisfied. [For $\omega_V = 0.2$ and $\omega_N = 0.95$, (13b) is exactly satisfied when $G(\mu)/\mu = 0.5$, that is, a canopy of random leaf orientation exposed to a near-nadir solar flux. In practice, $G(\mu)/\mu$ usually lies between 0.5 and 1.0, and ω_N is somewhat lower, so (13b) is still approximately satisfied.]

If the soil or background material is relatively dark, so that

$$\frac{\partial a_V}{\partial L_T} \to 0, \tag{14a}$$

SR will be mainly dependent on a_N, so

$$\frac{\partial(\text{SR})}{\partial L_T} \propto \frac{\partial a_N}{\partial L_T}, \tag{14b}$$

it follows then that FPAR is proportional to SR (Fig. 4).

The set of relationships set out in (12) through (14) applies to the case of a horizontally homogeneous canopy overlying a dark soil. Hall et al. (1990) carried out a parallel analysis on the case of clumped vegetation and again found that FPAR and a spectral vegetation index (SVI) were usually near-linearly related. In Sellers et al. (1992a), these two findings were examined, and it was shown that while SVI-L_T relationships may vary widely between vegetation morphologies, the relationships between SVI, FPAR, A_c, g_c, and albedo should be more conservative.

Lastly, Sellers et al. (1992a) posited that because the relationships SVI → FPAR → and nonstressed values of A_c, g_c were approximately linear they should be largely scale invariant. This means that to first order, *spatial averages* of SVI can theoretically be used to calculate *spatial integrals* of A_c and g_c. This should be true whether one considers a canopy varying in depth, a canopy varying in cover fraction, or a canopy that does both. This finding, which is partially supported by the analysis of FIFE data in Sellers et al. (1992b), is immensely useful in that it supports our use of coarse-resolution satellite SVI for the calculation of GCM grid-scale surface parameters and fluxes.

It should be remembered that the analysis described above and a large body of experimental evidence (see for example Hall et al. 1992) relate the SVI to the live green material in the canopy NL_T, rather than to the total (living plus nonliving) leaf area index L_T.

3. Datasets

a. The global 1° by 1° NDVI dataset

One year of data (1987) of the global 1° by 1° monthly composited normalized difference vegetation index (NDVI) dataset discussed by Los et al. (1994) was used to quantify both the spatial and temporal variability of land-surface parameters at monthly intervals, in particular of those related to vegetation. This 1° by 1° NDVI dataset was calculated from the first-generation Global Inventory, Monitoring, and Modeling Studies (GIMMS) continental NDVI datasets, which are based on Global Area Coverage (GAC) data (~5 km × 5 km) collected by channels 1 (red) and 2 (infrared) of the Advanced Very High Resolution Radiometer (AVHRR) on-board the NOAA environmental satellites. These datasets were initiated by Tucker et al. (1986) specifically for land-surface studies. Properties of the NOAA-AVHRR satellite-sensor system, such as the polar orbit of the satellite, the short interval between subsequent orbits, and the wide viewing angles, allow for data collection of the entire earth at almost daily intervals. For studies of the land surface, the objective is to composite cloud-free "clear" views of the surface, eliminating cloud-contaminated or otherwise dubious data. In most regions, the true temporal coverage of the land surface by AVHRR data is severely reduced by cloud cover obscuring the earth. Further limitations to the data are caused by scattering (molecules, aerosols) and absorption (ozone, water vapor) of radiation in the atmosphere, variations in the sensor viewing angle and illumination geometry, sensor degradation in channels 1 and 2 of the AVHRR, and variations in bidirectional reflectance properties of the earth's surface (Holben 1986; Los et al. 1994). Several steps are included in the processing of the continental NDVI data-

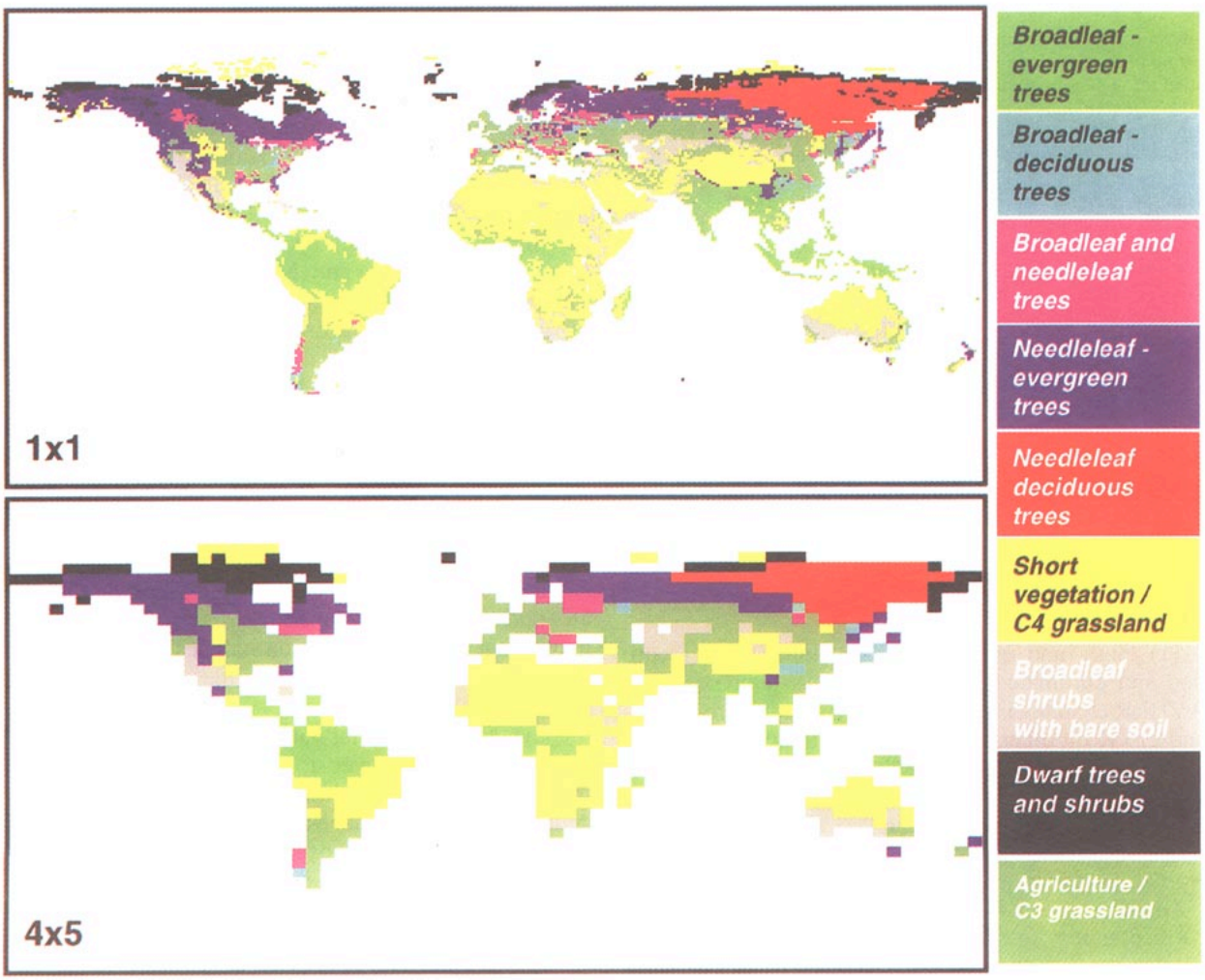

FIG. 5. Classification of the globe into nine major classes modified from the Matthews (1983) and Kuchler (1983) 1° by 1° land cover datasets and the Matthews land-use dataset (Matthews 1984), with modifications from Collatz and Berry (1992, personal communication). Data are also shown at 4° by 5° resolution as used by the SiB2-GCM in Randall et al. (1995).

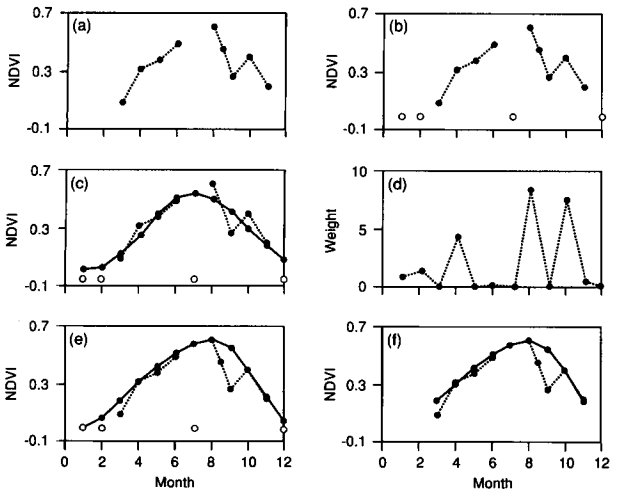

FIG. 6. Steps in the adjustment of NDVI time series with robust least-squares fitting of Fourier series [see items (i)–(vi) in section 4a]. (a) NDVI time series with four missing values and one outlier. (b) Missing values are substituted with NDVI = 0 prior to fitting of the Fourier series [see section 4a(i)]. Note that the original value for July is inconsistent with the rest of the time series. (c) Curve consisting of the first three harmonics (average, annual, biannual cycle) fitted through the data with least squares [(16)] [see section 4a(ii)]. (d) Weights calculated by comparing the fitted curve with the original data points. Values above the curve are assumed reliable (weights ≥ 1), values below the curve are assumed spurious [weights < 1; (17)], [see section 4a(iii)]. (e) Curve calculated with least squares using the weights under (d) (see section 4aiv). Note that points at months 3, 5, 7, and 9 are left out of the fitting procedure [(18)]. (f) Comparison of a newly calculated value against the original value and its four nearest neighbors to avoid overestimation [see sections 4a(v) and 4a(vi)]. Sequences of more than three missing values in the original data are set to missing values. These missing values are dealt with at a later stage in the FASIR procedure (sections 4c and 4d).

set to eliminate erroneous data and to reduce the effects of atmosphere, cloud remnants, and off-nadir viewing. A short description and an evaluation of the most important data processing steps are given below, more detailed discussions are provided in Holben (1986) and Los et al. (1994).

(i) High- and medium-altitude clouds were identified and eliminated by the brightness temperature in AVHRR channel 5 with a threshold of 288 K for Africa and 273 K for other continents. This temperature-based threshold does not eliminate data from warm clouds or subpixel-size clouds. In addition, data from areas with surface temperatures less than 273 K were eliminated, resulting in missing data for high latitudes in the Northern Hemisphere during winter.

(ii) The outer 45 pixels on either side of a scan, corresponding to viewing angles of about 42° or greater, were eliminated to avoid large variations in the data as a result of illumination and viewing geometry. Effects of increased atmospheric path lengths and surface bidirectional reflectance distribution function (BRDF) effects as a result of larger solar zenith angles were not eliminated by this cutoff.

(iii) A preflight calibration of channel 1 and 2 data as specified by NOAA (Kidwell 1991) was applied. This preflight calibration includes a normalization in each band for the intensity of incoming solar radiation.

(iv) The NDVI was calculated from the selected channel 1 and 2 reflectance values and mapped by continent on a stereographic projection. Because of limitations in data storage and processing capacity, no information on individual channel data was retained.

(v) The maximum NDVI value for each month was selected for each pixel to obtain monthly maximum value composites. Because atmospheric scattering, absorption, and clouds all act to reduce the NDVI, selecting maximum values increases the contribution of data collected under cloud-free, clear-sky conditions (Holben 1986). In the case of persistent cloud or other atmospheric effects, spurious data remain: for example, Eck and Kalb (1991) reported on the presence of cloud-contaminated data not eliminated by either the temperature threshold or compositing technique in this dataset; Justice et al. (1991) reported decreased NDVI values in the Sahel at the start of the growing season due to the movement of humid air masses into the region associated with the migration of the intertropical convergence zone (ITCZ); and Tucker and Matson (1985) and Vermote et al. (1994) described the effect of atmospheric aerosols on the NDVI after the eruptions of El Chichón and Mt Pinatubo, respectively. Maximum value compositing tends to favor selection of data from the forward-scatter direction [10° in the forward-scatter direction on average, with 50% of the data between around 10° in the backscatter direction and 30° in the forward-scatter direction; see Gutman (1991)] instead of near-nadir views as was previously assumed (Holben 1986). However, after averaging the NDVI data to 1° by 1°, the variation in the NDVI as a result of view angle effects is likely to be small.

(vi) The effect of sensor degradation in AVHRR channels 1 and 2 on the NDVI was accounted for by an approximation developed by Los (1993). It is estimated that this approximation reduces biases between data segments taken at different times to less than 0.002 units of NDVI.

(vii) The continental datasets are resampled by averaging the pixels over 1° by 1°. Surface water and missing values are excluded from the averaging procedure. Averaging reduces the impact of random errors and in part cancels the effect of minor errors with opposite signs. Minor errors may be produced from a positive bias in the NDVI due to compositing, variations in the NDVI caused by the spectral properties of the soil background, NDVI dependence on view angle, and the effects of inaccuracies in registration and mapping of AVHRR data. These errors are thought to be relatively small and, in any case, are impossible to account

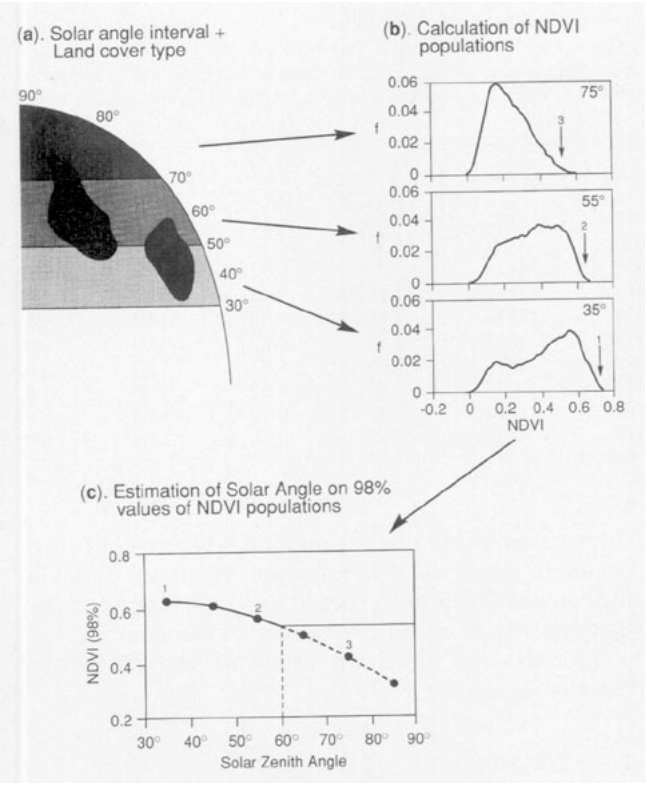

FIG. 7. Schematic of analysis procedure applied to the Fourier-adjusted data (FA) to extract the dependence of observed maximum NDVI (full green canopy) on solar zenith angle. (a) For each monthly dataset, the globe is divided into solar zenith angle classes (the situation for the Northern Hemisphere equinox is shown as an example so that the solar zenith angle intervals correspond to latitude bands), for solar zenith angle correction. (b) The set of solar zenith angles is combined with the set of vegetation types to produce populations of Fourier-adjusted NDVI data (by solar zenith angle and vegetation type). The 98 percentile of each population is assumed to correspond to a full green canopy. (c) The 98 percentile points for each vegetation type are plotted against solar zenith angle and a simple empirical function is fitted [see (19) and (21) in the text]. Numbers in plot (b) correspond to numbers in plot (c).

for without access to the component AVHRR channel 1 and 2 data.

An estimate of the magnitude of errors in the 1° by 1° NDVI data is given in Los et al. (1994).

b. *Stratification of the NDVI data into land-cover types*

A land-cover stratification scheme was used to account for the dependency of the relationships between NDVI, land-surface parameters, and vegetation type. The land-cover classification used for this study is based on the Matthews land-cover and land-use datasets (Matthews 1983, 1984, 1985) and the Kuchler (1983) land-cover dataset. Both the Matthews and Kuchler datasets have a resolution of 1° by 1° and distinguish 32 main land-cover types (Table 2). The original SiB1 vegetation classification of Dorman and Sellers (1989) was based on these Matthews and Kuchler datasets. The 1° by 1° SiB1 classification was used to process the satellite data, in particular to carry out the solar zenith angle correction and reconstruction procedures described in section 4. To accommodate the new photosynthesis–conductance model, the two vegetation layers in SiB1 were reduced to one layer in SiB2, which also involved reducing the number of vegetation classes from 12 to 9 (see Table 2; Sellers et al. 1995). The nine SiB2 vegetation classes shown in Table 2 and Fig. 5 are used to assign surface parameter values.

The basis of this final land-cover dataset is the Matthews dataset. Some modifications were made to obtain closer agreement with the classes and the SiB2 biomes for which the vegetation parameters in Table 5 were established:

(i) for South America, the Kuchler classification replaced the Matthews classification;

(ii) in North America, the Kuchler land-cover-type 4 (needleleaf evergreen) replaced the Matthews classification;

(iii) in Siberia, Kuchler vegetation-type 5 (needleleaf deciduous, mainly larix species) replaced the Matthews classification, because the Matthews classification does not make a distinction between broadleaf and needleleaf deciduous cover types;

(iv) in cases where a grid cell contained over 50% agricultural activity as defined in the Matthews land-use dataset, class 9 (agriculture) was assigned (Dorman and Sellers 1989);

(v) the Kuchler and Matthews classes were merged to reflect either a C_3 or C_4 cover type: SiB2 class 6 (SiB1 classes 6, 7, 8 and 11) was used to represent C_4 types and SiB2 class 9 (SiB1 class 12 at the 1° by 1° scale) was used to represent C_3 types. A more realistic distribution of C_3 and C_4 types at the 1° by 1° scale will be used for future studies (Collatz and Berry 1992, personal communication).

The SiB2 land-cover classification is depicted in Fig. 5.

4. An adjusted NDVI product: FASIR-NDVI

To correct the global 1° by 1° NDVI dataset for the errors discussed in section 3a, a series of adjustments was developed, collectively referred to as FASIR, which stands for

- Fourier wave Adjustment,
- Solar zenith angle adjustment,
- Interpolation of missing data, and
- Reconstruction of NDVI data classified as tropical evergreen broadleaf.

Prior to the Fourier wave adjustment, remnants of the terminator effect that were marked by erroneous NDVI

TABLE 3. Vegetation-cover types with examples of the associated properties: maximum leaf area index, $L_{T,\max}$, stem area index, L_s, NDVI at 98% and 5% of NDVI distributions, parameters for the solar zenith angle correction k_1 through k_4 [see (19) and (20)], and the fraction of clumped vegetation, F_{cl} [(25)]. For the solar angle correction only, a distinction is made within SiB2 biome 6 between the old SiB1 biome 6, which is treated as morphologically similar to class 1, and SiB1 biomes 7, 8, and 11, which are treated as morphologically similar to the short vegetation classes.

SiB2 biome	$L_{T,\max}$	L_s	$NDVI_{98\%}$	$NDVI_{5\%}$	k_1	k_2	k_3	k_4	F_{cl}
1	7	0.08	0.611	0.039	0.15	2.80	0.52	1.04	0.0
2	7	0.08	0.721	0.039	0.32	1.38	0.52	1.04	0.0
3	7.5	0.08	0.721	0.039	0.28	1.35	0.52	1.04	0.5
4	8	0.08	0.689	0.039	0.19	1.18	0.52	1.04	1.0
5	8	0.08	0.689	0.039	0.19	1.18	0.52	1.04	1.0
6-6	5	0.05	0.611	0.039	0.15	2.80	0.52	1.04	0.0
6-other	5	0.05	0.674	0.039	0.38	1.45	0.52	1.04	0.0
7	5	0.05	0.674	0.039	0.38	1.45	0.52	1.04	1.0
8	5	0.05	0.674	0.039	0.38	1.45	0.52	1.04	0.0
9	5	0.05	0.674	0.039	0.38	1.45	0.52	1.04	0.0

values (Holben 1986) were eliminated by discarding all data associated with solar zenith angles larger than 85°. The FASIR procedures were first described in Sellers et al. (1994).

a. *FASIR: Fourier wave adjustment of NDVI time series*

The adjustment of outliers in the NDVI time series using Fourier series analysis is based on two assumptions: first, the NDVI time series should be smoothly varying at any given point; and second, the major sources of error defined earlier can only decrease the value of the NDVI. The first assumption is used to identify short-term irregularities ($\leq$2 months) in time series that could be the result of persistent cloud cover or atmospheric effects (water vapor, aerosols). The second assumption has been used for some time now to justify the calculation of monthly maximum value composites (Holben 1986; Tucker et al. 1986). There are some cases where this assumption will not hold (discussed in Los et al. 1994), but the effects are trivial in the context of this analysis and generally much smaller than the effects of the atmosphere or clouds.

Fourier series are a summation of sine and cosine functions given by

$$\hat{Y}_i = \sum_{j=1}^{m} a_j \cos[(j-1)\phi_i] + b_j \sin[(j-1)\phi_i], \tag{15}$$

where a and b are Fourier coefficients;

$$\phi_i = 2\pi(i-1)/n$$

the phase; i ranges from 1 to n; $n = 12$ is the number of points in the sequence; and $m = 3$ is the number of harmonics. The selection of $m = 3$ meets the requirement of smoothness and at the same time incorporates a large part of the seasonal variation in the NDVI. The correction is limited to less than a sequence of outliers

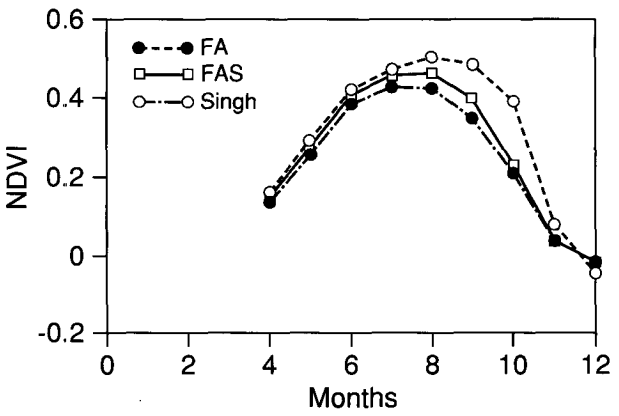

FIG. 8. Illustration of the solar zenith angle correction for a Fourier-adjusted (FA) NDVI time series of a region in the boreal forest (50.5°N, 88.5°W). The Singh (1988) solar angle correction is shown for comparison.

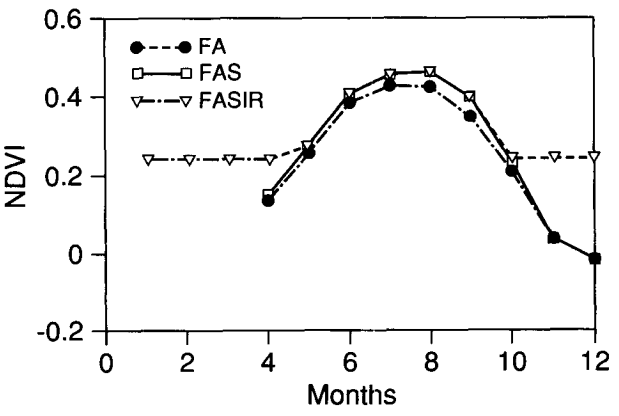

FIG. 9. Example of interpolation for the Fourier-adjusted and solar zenith angle corrected evergreen needleleaf NDVI data of Fig. 8 during the Northern Hemisphere winter (50.5°N, 88.5°W).

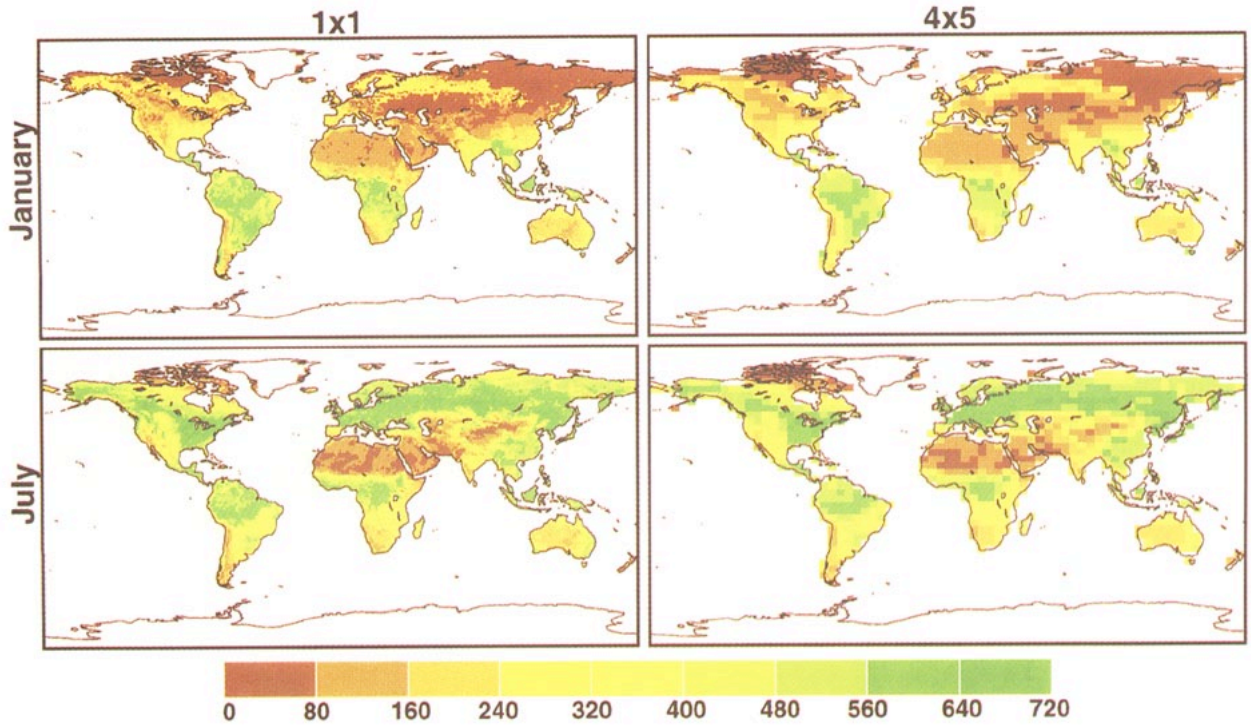

FIG. 10. FASIR-NDVI (values are multiplied by 1000) for (top) January 1987 and (bottom) July 1987. Comparison with the NDVI data published by Los et al. (1994) shows overall increased values for green biome-types during their growing season (Fig. 24). For the winter, NDVI data from evergreen needleleaf biome-types are restored by the interpolation (FASI) procedure.

of $n/2^{m-1}$ data points in a row, hence for $m = 3$, a sequence of 3 or more outliers will erroneously be incorporated in the adjusted series.

A robust least-squares optimizing method was used to identify and adjust outliers from the general trend in the NDVI time series. Robust least-squares methods are designed to eliminate data that deviate strongly from a general trend and could distort the analysis (Hoaglin et al. 1983). These methods are generally iterative, and in successive cycles residuals are weighted as a function of the distance from the fitted curve. A modification to the robust least squares optimizing technique was made to take into account the assumption that errors in the NDVI result in decreased values, hence negative deviations from the fitted curve receive low weights during fitting and positive deviations receive high weights.

The general processing scheme for the Fourier-adjustment procedure is discussed here and shown schematically in Fig. 6. A broad outline is as follows:

(i) Values are substituted for missing data points prior to fitting the Fourier series. Because the majority of missing values occur during periods of low surface temperature and therefore low greenness values, a low NDVI value, NDVI = 0 is inserted (Fig. 6b);

(ii) The Fourier series are fitted through the data using the least-squares method (Fig. 6c),

$$(\mathbf{F}^{\mathrm{T}}\cdot\mathbf{F})\cdot\mathbf{c} = \mathbf{F}^{\mathrm{T}}\cdot\mathbf{Y}, \tag{16}$$

where the observed data are

$$\mathbf{Y} = \begin{bmatrix} Y_1 \\ \vdots \\ Y_n \end{bmatrix}$$

and the Fourier constants to be solved are

$$\mathbf{c} = \begin{bmatrix} c_1 \\ \vdots \\ c_{2m-1} \end{bmatrix}$$

and

$$\mathbf{F} = \begin{bmatrix} 1 & \cos(\phi_1) & \sin(\phi_1) & \cos(2\phi_1) & \sin(2\phi_1) \\ & & \vdots & & \\ 1 & \cos(\phi_n) & \sin(\phi_n) & \cos(2\phi_n) & \sin(2\phi_n) \end{bmatrix}.$$

(iii) The weights, W_i, are calculated according to distance from the fitted curve (Fig. 6d)

$$W_i = \begin{cases} 0, & \text{if } U_i \leq -k \\ [1 + (U_i + r)/k]^4, & \text{if } -k < U_i < -r \\ 1, & \text{if } -r \leq U_i \leq r \\ [1 + (U_i - r)/k]^2, & \text{if } U_i > r \end{cases} \quad (17)$$

and

$$0 \leq W_{i=1} \leq 1$$

$$0 \leq W_{i=n} \leq 1,$$

where $U = (Y - \hat{Y})/M$; M is the median of the absolute difference values of Y and $\hat{Y}$; $k = 2$; and $r = M/20$.

(iv) Fourier series are fitted through the data using (16), now with the weights W taken into account (Fig. 6e):

$$(\mathbf{F}_W^{\mathrm{T}} \cdot \mathbf{F}_W) \cdot \mathbf{c} = \mathbf{F}_W^{\mathrm{T}} \cdot \mathbf{Y}_W, \quad (18)$$

where

$$\mathbf{Y}_W = \begin{bmatrix} W_1 Y_1 \\ \vdots \\ W_n Y_n \end{bmatrix}$$

and

$$\mathbf{F}_W = \begin{bmatrix} W_1 & & W_1 \cos(2\phi_1) & W_1 \sin(2\phi_1) \\ & \ddots & & \\ W_n & & W_n \cos(2\phi_n) & W_n \sin(2\phi_n) \end{bmatrix}.$$

(v) Each point is then checked against its original value and the values of its four nearest neighbors ($i - 2, i - 1, i, i + 1, i + 2$). The new value is constrained not to exceed the maximum of the five original values by more than 2% or to be lower than the original value (Fig. 6f). Note that the series is cyclic, hence the neighbors to the right for $i = 12$ are $i = 1$ and $i = 2$;

(vi) Sequences of three or more missing values in the original data are set to missing values after adjustment of the data to avoid inclusion of suspect data (Fig. 6f). The missing values are dealt with by the interpolation and reconstruction techniques, see below.

b. *FASIR: Solar zenith angle correction*

The NDVI varies with solar zenith angle as a result of increased atmospheric path lengths and surface BRDF effects. Studies on the BRDF properties of vegetation have for the most part been carried out over uniform cover types at the plot scale (Kimes 1983; Holben et al. 1986; Deering et al. 1992). Little work has been done to translate the results from ground measurements to observations made at the top of the atmosphere. Lacking a calibrated, physically based model, a simple empirical procedure was used to account for solar zenith angle effects. First, we analyzed the entire NDVI dataset to identify a set of dense green vegetation covers for four vegetation morphologies (grass–crops, broadleaf evergreen forests, broadleaf deciduous forests, coniferous forests) that were exposed to a range of solar zenith angles (20°–70°), see below. Solar zenith angles were calculated assuming a nadir view angle for the fifteenth day of each month for an equatorial satellite crossing time according to Price (1991) and for orbits as described in Kidwell (1991). The monthly NDVI data were stratified by vegetation morphology and solar zenith angle interval (see Fig. 7). These stratified datasets were then combined into annual sets; for example, data from a broadleaf evergreen type in the Southern Hemisphere collected during December were combined with data from a broadleaf evergreen type on the Northern Hemisphere collected during July having the same solar zenith angle interval. The 98% values of these combined NDVI distributions were then assumed to represent conditions of green, maximum-density vegetation cover. These 98% values were plotted against solar zenith angle, and a curve was fitted through the data using the form of the equation derived by Singh (1988):

$$y_{98} = k_1(\theta - \pi/6)^{k_2}, \quad (19)$$

with $y = (\mathrm{NDVI}_{98,0} - \mathrm{NDVI}_\theta)/\mathrm{NDVI}_{98,0}$, where $\mathrm{NDVI}_{98,0}$ represents 98% of the NDVI distribution for a particular class (i.e., the greenest values) as observed for a zero solar zenith angle. A similar procedure was developed to describe the effect of solar zenith angle on bare soil. It was assumed that the lowest 5% values for bare soil and shrubs (class 7) and bare soil classes (deserts in class 6) represented no-vegetation conditions. The 5% values were extracted and plotted versus solar zenith angle to obtain

$$y_5 = k_3(\theta - \pi/6)^{k_4}, \quad (20)$$

with $y = (\mathrm{NDVI}_\theta - \mathrm{NDVI}_{5,0})/\mathrm{NDVI}_{5,0}$. The parameters k_1 through k_4 were estimated with least squares. Values of parameters k_1 through k_4 for each land-cover class are set out in Table 3. If no data were available for a vegetation type for solar zenith angles smaller than 30°, a small number, NDVI = 0.008, was added to the maximum (98%) NDVI values obtained between 30° and 60° solar zenith angle to allow fitting of (19) and (20).

With the relationships between NDVI and solar zenith angle established for high and low NDVI values, the equivalent "overhead sun" value NDVI_0 for an intermediate NDVI for any solar zenith angle is calculated by

$$\mathrm{NDVI}_0 = \frac{(\mathrm{NDVI}_\theta - \mathrm{NDVI}_{5,\theta})(\mathrm{NDVI}_{98,0} - \mathrm{NDVI}_{5,0})}{(\mathrm{NDVI}_{98,\theta} - \mathrm{NDVI}_{5,\theta})} + \mathrm{NDVI}_{5,0}. \quad (21)$$

Equation (21) assumes a linear variation of the solar zenith angle correction to NDVI over the considered range of NDVI. The solar zenith angle correction is

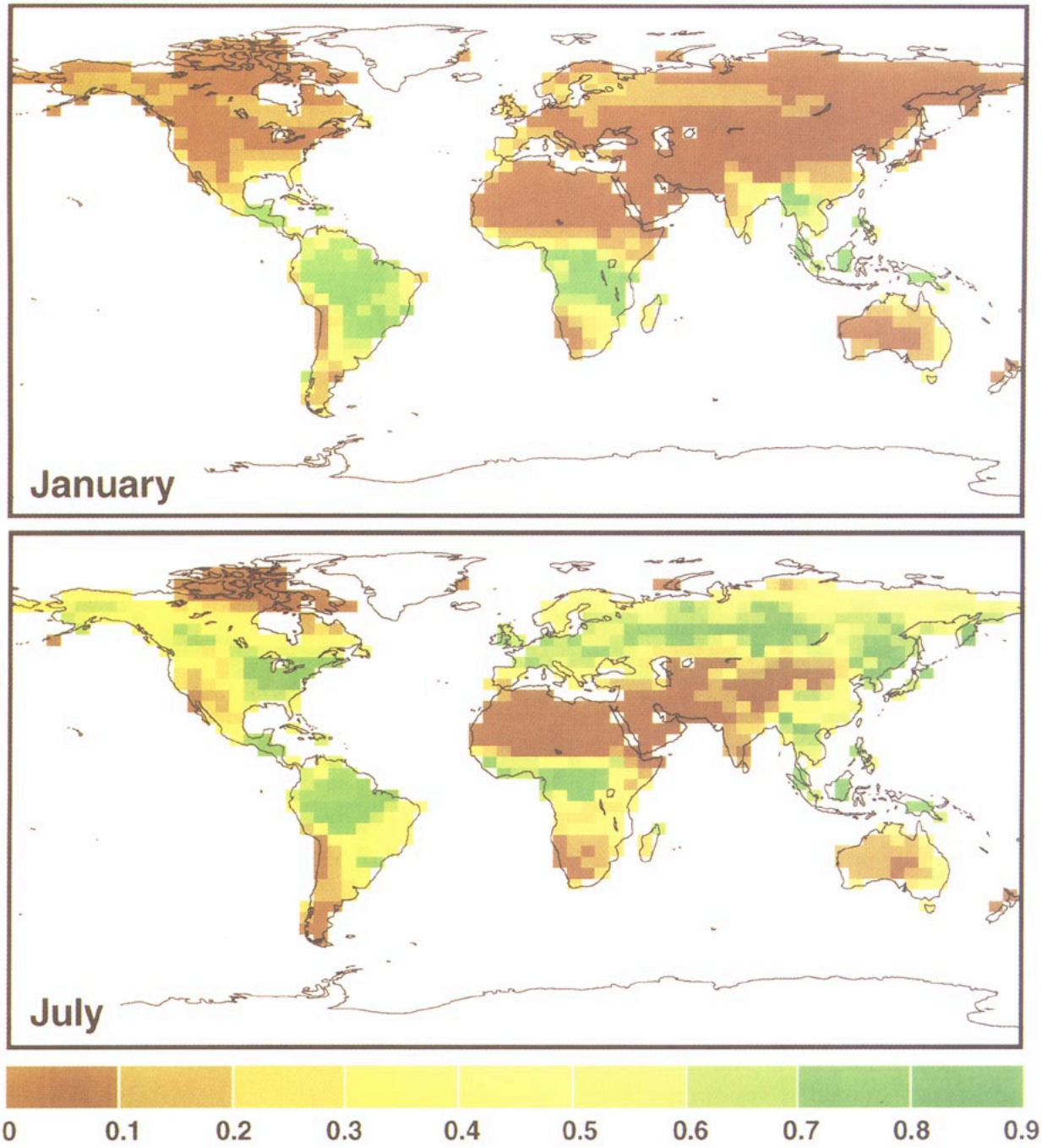

FIG. 11. Fields of FPAR for (top) January and (bottom) July 1987 calculated from the FASIR-NDVI data.

applied to zenith angles of up to 60° and then held constant for higher angles, (see Fig. 7). The effect of our solar zenith angle correction on the time series is shown in Fig. 8 for a midlatitude area, with a similar correction for solar zenith angle developed by Singh (1988) shown for comparison; our correction is more conservative, especially for high solar zenith angles.

c. FASIR: Interpolation of missing data

The original NDVI dataset of Los et al. (1994) contains data dropouts (missing values) whenever the surface radiative temperature falls below 273 K (288 K for Africa). These missing values present a significant problem at high latitudes during the

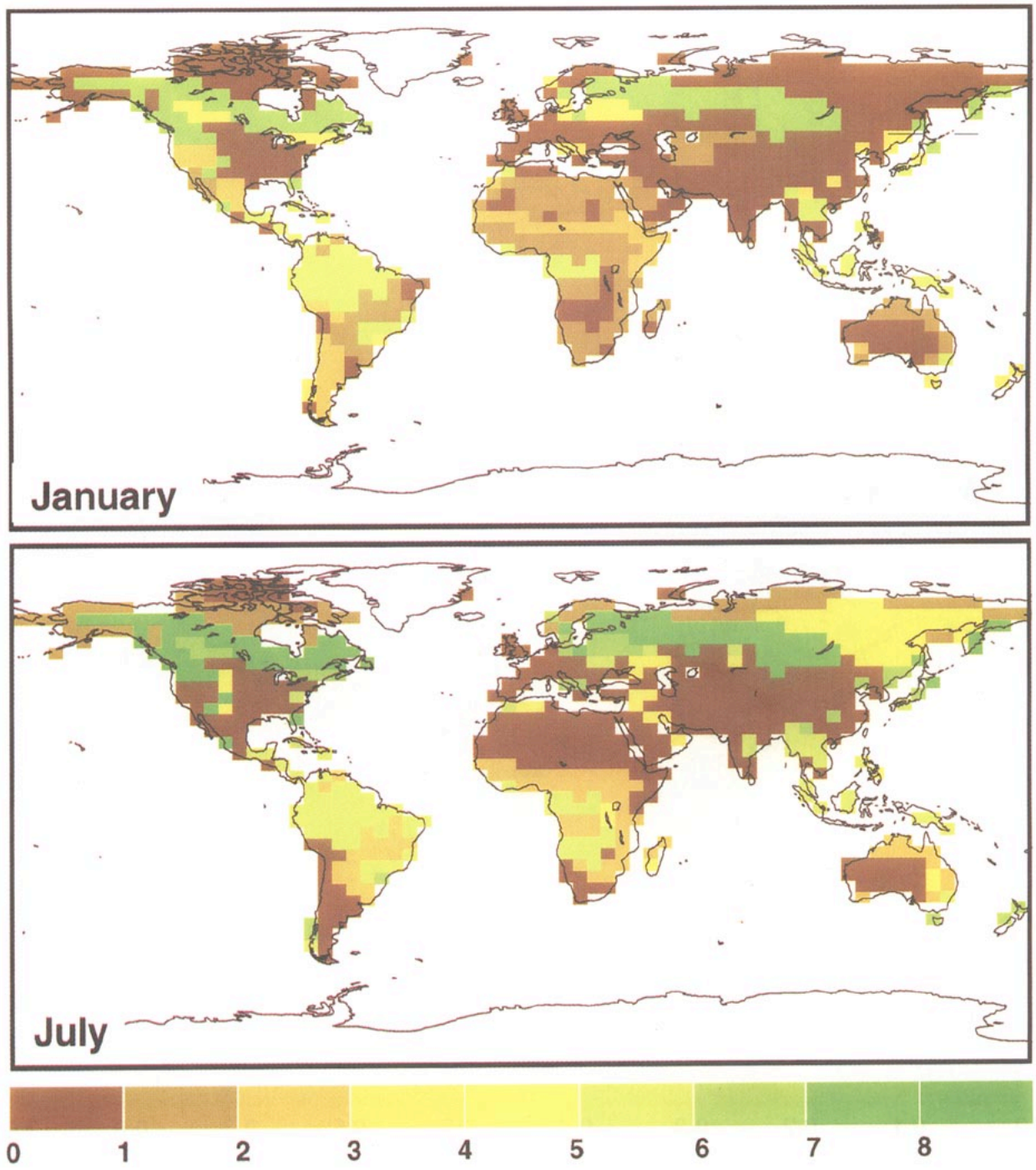

FIG. 12. Fields of total leaf area index (L_T) for (top) January and (bottom) July as specified for the original SiB1 model of Sellers et al. (1986). The L_T fields were assigned as monthly varying values for each vegetation type (with a six-month phase change for the Southern Hemisphere) (see Dorman and Sellers 1989 for details).

Northern Hemisphere winter because, given a spurious NDVI of zero, SiB2 will calculate erroneous albedo and roughness length values. This would be particularly damaging for forest areas because no vegetation would be assigned to an area where trees might project through the snow and influence the albedo and surface roughness. The Fourier-adjustment procedure only allows for restoration of oc-

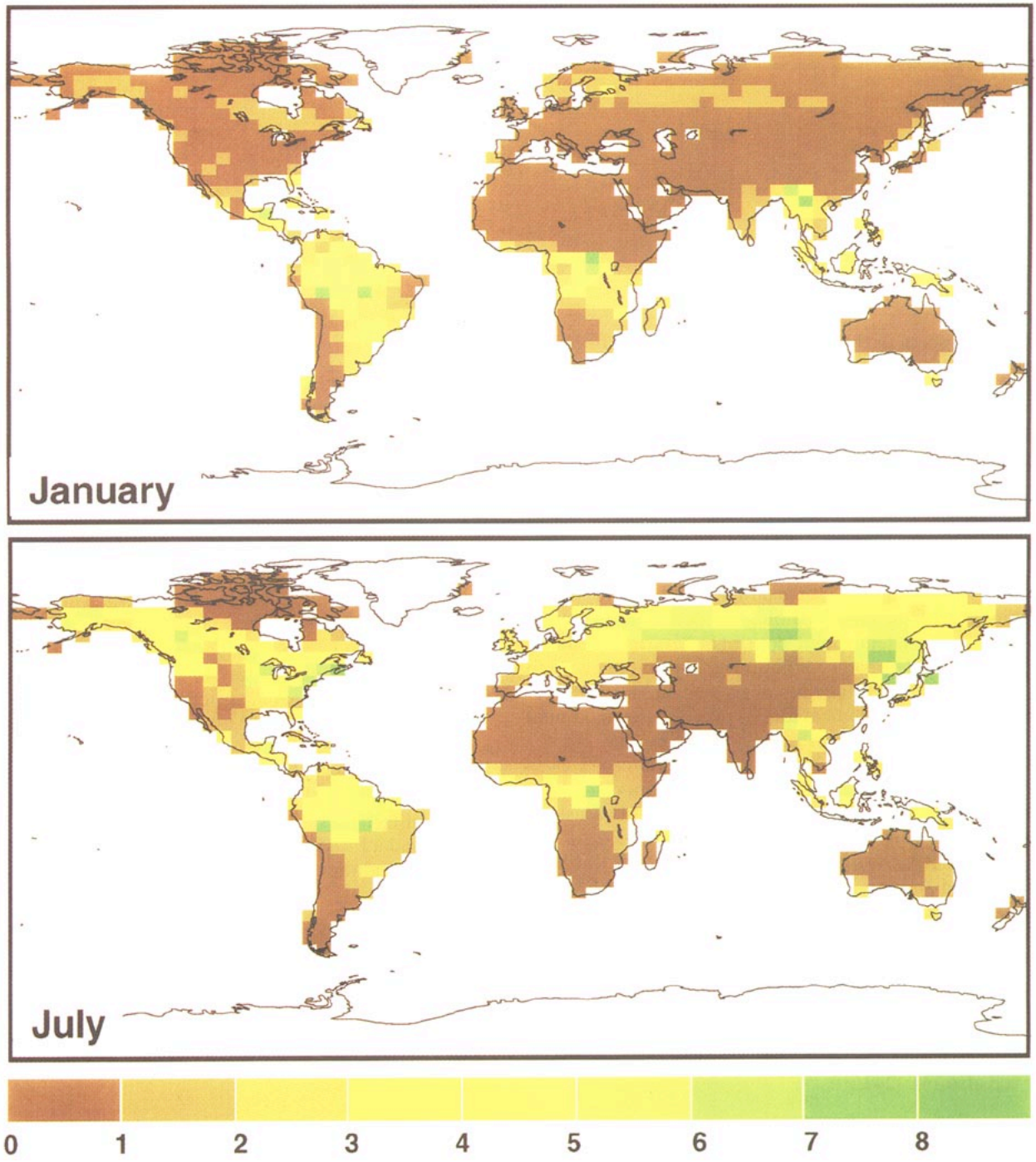

FIG. 13. Fields of leaf area index (L_T) for (top) January and (bottom) July 1987 as calculated from the FASIR-NDVI dataset [(6), (7), and (8)].

currences of fewer than three missing NDVI values in a row. To get around this problem of several successive missing NDVI values, a best guess is made about the "effective winter" NDVI value of evergreen needleleaf vegetation by selecting a value at the end of the growing season when the only remaining green component is assumed to be evergreen. For this study, the NDVI value of October is used to replace missing values in areas covered with needleleaf evergreen vegetation during winter. A similar procedure, with a six-month phase shift, was followed for missing

TABLE 4. Soil texture types, as defined in the global map by Zobler (1986), matched with soil physical parameters from Clapp and Hornberger (1978). Here B is soil wetness exponent, Ψ_s is soil tension at saturation (m), K_s is hydraulic conductivity at saturation (m s^{-1}), θ_s is soil porosity (volume fraction) (see Table 6).

Class	B	Ψ_s	$K_s \times 10^6$	θ_s	Description
1	4.05	−0.04	176.0	0.40	Sand
2	4.90	−0.07	35.0	0.44	Sandy loam
3	5.39	−0.15	7.0	0.45	Loam
4	7.12	−0.12	6.3	0.42	Clay loam → sandy clay loam
5	8.52	−0.36	2.5	0.48	Clay → clay loam
6	4.05	−0.04	176.0	0.40	Ice
7	5.39	−0.15	7.0	0.45	Organic

winter values in the Southern Hemisphere. Figure 9 shows an example of the interpolation of missing values.

d. FASIR: Reconstruction of NDVI time series over tropical regions

The Fourier-adjusted NDVI time-series over the Tropics show incontrovertible evidence of serious cloud contamination, for example, low NDVI values coinciding with the climatological occurrence of rainfall and persistent cloud cover (Sellers and Schimel 1993). Our temporary solution to this problem is to raise the NDVI values for evergreen broadleaf vegetation (class 1 or tropical forest) pixels to the maximum observed for that pixel during the year. The class 9 (drought-deciduous broadleaf) of the source 32 class Matthews land-cover data is excluded from class 1 for this procedure because it is a class with highly seasonal vegetation. It is marked by brackets in Table 2.

Figure 10 shows global FASIR-NDVI data for February and August 1987. When comparing the FASIR-NDVI data with the 1° by 1° NDVI dataset of Los et al. (1994), it can be seen that the former dataset has higher values over green areas, where we expect the largest impacts due to atmosphere effects and clouds; similar values over deserts, where we expect atmospheric perturbations to be of minor importance; and nonzero values for the boreal forest during the winter (see also Fig. 24).

5. Calculation of FPAR, leaf area index (L_T), and canopy greenness fraction (N) from FASIR-NDVI

The FASIR-NDVI is taken to be indicative of the amount of green material in the vegetation canopy. FPAR and the green leaf area index NL_T are calculated from the NDVI using simple relationships discussed earlier. The total leaf area index, L_T, and the canopy greenness fraction, N, are then calculated from analysis of time series of NL_T.

a. Calculation of FPAR from FASIR-NDVI

The theoretical relation between FPAR and SR [which is a simple transformation of NDVI; SR = (1 + NDVI)/(1 − NDVI)] was shown to be near-linear in the work of Sellers et al. (1992a). Analysis of field data gathered over a range of spatial scales over a Kansas grassland confirmed the near-linearity of this relationship, at least for homogeneous vegetation covers with dark soil backgrounds (see Sellers et al. 1992b; Hall et al. 1992; and Fig. 4).

Assuming linearity, the equation for SR and FPAR can be solved when two points are known. These two points were established using a simple analysis of the NDVI data populations discussed in section 4b and shown as histograms in Fig. 7b. The 98% NDVI for tall vegetation types and agriculture is assumed to represent vegetation at full cover and maximum activity with a FPAR value close to 1 (here assumed to be 0.950). The 98% NDVI value of agriculture was used to represent all short vegetation types. The 5% desert value is assumed to represent no vegetation activity and a FPAR value of 0.001 for all land-cover types. The relation between FPAR and SR is then given by

$$\mathrm{FPAR} = \frac{(\mathrm{SR} - \mathrm{SR}_{i,\min})(\mathrm{FPAR}_{\max} - \mathrm{FPAR}_{\min})}{(\mathrm{SR}_{i,\max} - \mathrm{SR}_{i,\min})} + \mathrm{FPAR}_{\min}, \quad (22)$$

where

$\mathrm{FPAR}_{\max} = 0.950$;
$\mathrm{FPAR}_{\min} = 0.001$,
$\mathrm{FPAR}_{\max}$, $\mathrm{FPAR}_{\min}$ independent of vegetation type;
$\mathrm{SR}_{i,\max}$ = SR value corresponding to 98% of NDVI population i;
$\mathrm{SR}_{i,\min}$ = SR value corresponding to 5% of NDVI population i.

The land-cover type-dependent NDVI values for 98% and 5% of data populations can be found in Table 3. Note that the 5% and 98% values are the same values used for the solar zenith angle correction and are tied to the same vegetation classification.

TABLE 5. Time-invariant land-surface properties. Most of these are used in the preprocessor (MAPPER) to calculate parameter fields for SiB2. Very few are used directly in the GCM.

Parameter	Definition	Units	Values by biome 1	2	3	4	5	6	7	8	9
(a) Biome-dependent morphological, optical and physiological parameters.											
Morphological properties											
z_2	Canopy-top height	m	35.0	20.0	20.0	17.0	17.0	1.0	0.5	0.6	1.0
z_1	Canopy-base height	m	1.0	11.5	10.0	8.5	8.5	0.1	0.1	0.1	0.1
z_c	Inflection height for leaf-area density	m	28.0	17.0	15.0	10.0	10.0	0.55	0.3	0.35	0.55
V	Canopy-cover fraction	—	1.0	1.0	1.0	1.0	1.0	1.0	0.1	1.0	1.0
χ_L	Leaf-angle distribution factor	—	0.1	0.25	0.125	0.01	0.01	−0.3	0.01	0.2	−0.3
l_w	Leaf width	m	0.05	0.08	0.04	0.001	0.001	0.01	0.003	0.01	0.01
l_l	Leaf length	m	0.1	0.15	0.1	0.055	0.04	0.3	0.03	0.3	0.3
D_T	Total soil depth	m	3.5	2.0	2.0	2.0	2.0	1.5	1.5	1.5	1.5
D_r	Root depth	m	1.5	1.5	1.5	1.5	1.5	1.0	1.0	1.0	1.0
Optical properties											
$\alpha_{V,l}$	Leaf reflectance, visible, live	—	0.1	0.1	0.07	0.07	0.07	0.105	0.1	0.105	0.105
$\alpha_{V,d}$	Leaf reflectance, visible, dead	—	0.16	0.16	0.16	0.16	0.16	0.36	0.16	0.36	0.36
$\alpha_{N,l}$	Leaf reflectance, near IR, live	—	0.45	0.45	0.4	0.35	0.35	0.58	0.45	0.58	0.58
$\alpha_{N,d}$	Leaf reflectance, near IR, dead	—	0.39	0.39	0.39	0.39	0.39	0.58	0.39	0.58	0.58
$\delta_{V,l}$	Leaf transmittance, visible, live	—	0.05	0.05	0.05	0.05	0.05	0.07	0.05	0.07	0.07
$\delta_{V,d}$	Leaf transmittance, visible, dead	—	0.001	0.001	0.001	0.001	0.001	0.22	0.001	0.22	0.22
$\delta_{N,l}$	Leaf transmittance, near IR, live	—	0.25	0.25	0.15	0.1	0.1	0.25	0.25	0.25	0.25
$\delta_{N,d}$	Leaf transmittance, near IR, dead	—	0.001	0.001	0.001	0.001	0.001	0.38	0.001	0.38	0.38
a_{sV}	Soil reflectance, visible	—	0.11	0.11	0.11	0.11	0.11	[a]	[a]	0.11	0.1
a_{sN}	Soil reflectance, near IR	—	0.225	0.225	0.225	0.225	0.225	[a]	[a]	0.225	0.15
Physiological properties											
V_{max_0}	Maximum rubisco capacity, top leaf	mol m^{-2} s^{-1}	1×10^{-4}	1×10^{-4}	8×10^{-5}	6×10^{-5}	1×10^{-4}	3×10^{-5}	6×10^{-5}	6×10^{-5}	1×10^{-4}
ϵ	Intrinsic quantum efficiency	mol mol^{-1}	0.08	0.08	0.08	0.08	0.08	0.05	0.08	0.08	0.08
m	Stomatal slope factor	—	9.0	9.0	9.0	9.0	9.0	4.0	9.0	9.0	9.0
b	Minimum stomatal conductance	mol m^{-2} s^{-1}	0.01	0.01	0.01	0.01	0.01	0.04	0.01	0.01	0.01
β_{ce}	Photosynthesis coupling coefficient	—	0.98	0.98	0.98	0.98	0.98	0.8	0.98	0.98	0.98
s_2	High temperature stress factor, photosynthesis	K	313	311	307	303	303	313	313	303	308
s_4	Low temperature stress factor, photosynthesis	K	288	283	281	278	278	288	283	278	281
ψ_c	One-half inhibition water potential	m	−200	−200	−200	−200	−200	−200	−300	−200	−200
f_d	Leaf respiration factor	—	0.015	0.015	0.015	0.015	0.015	0.025	0.015	0.015	0.015

[a] Soil reflectance for grid cells designated as bare soil within biomes 6 and 7 are specified according to ERBE data.

Parameter	Description	Units	Value
(b) Biome independent morphological and physiological parameters.			
Morphological parameters			
z_s	Ground roughness length	m	0.05
G_1	Augmentation factor for momentum transfer coefficient	—	1.449
G_4	Transition height factor for momentum transfer coefficient	—	11.785
D_1	Depth of surface soil layer	m	0.02
$\varnothing_s$	Mean topographic slope	radians	0.176
Physiological parameters			
S	Rubisco specificity for CO_2 relative to O_2	—	2600×0.57^{Qt}
K_c	Rubisco Michaelis–Menten constant for CO_2	Pa	30×2.1^{Qt}
K_o	Rubisco inhibition constant for O_2	Pa	$30\,000 \times 1.2^{Qt}$
β_{ps}	Photosynthesis coupling coefficient	—	0.95
s_1	High temperature stress factor, photosynthesis	K^{-1}	0.3
s_3	Low temperature stress factor, photosynthesis	K^{-1}	0.2
s_5	High temperature stress factor, respiration	K^{-1}	1.3
s_6	High temperature stress factor, respiration	K	328
Q_t	Q_{10} temperature coefficient	—	$(T_c - 298)/10$

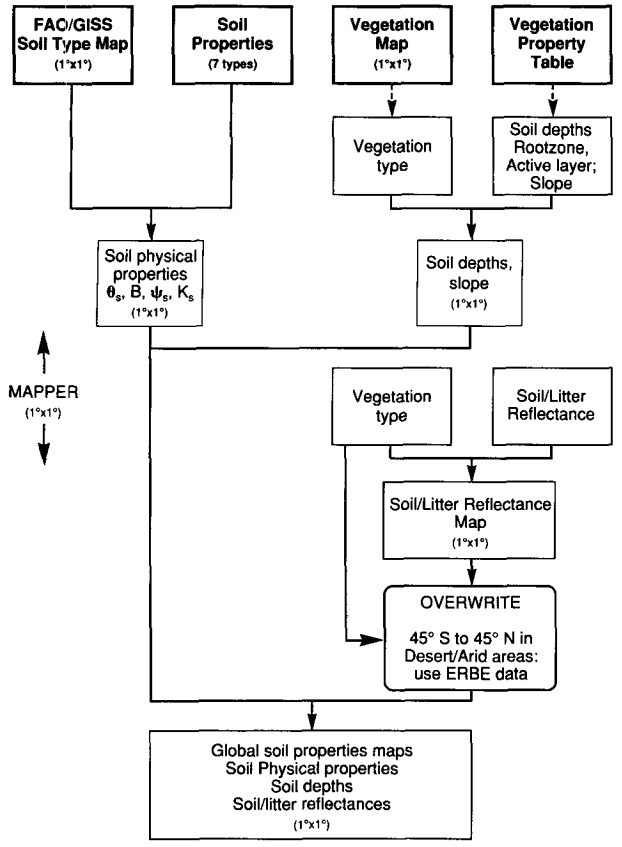

FIG. 14. Schematic of procedures used to generate global fields of soil properties for use in SiB2. All of these procedures are conducted off-line (i.e., prior to the GCM run) in the MAPPER preprocessor program.

b. *Calculation of green leaf area index, $L_g = NL_T$, from FPAR*

The relationship between FPAR and the green leaf area index L_g can be described by an exponential equation (Monteith and Unsworth 1990)

$$L_g = L_{g,i,\max} \frac{\log(1 - \text{FPAR})}{\log(1 - \text{FPAR}_{\max})}, \quad (23)$$

where $L_{g,i,\max}$ is the maximum green leaf area index defined for vegetation type i. The equation was derived at local levels and is found to be valid for evenly distributed vegetation at regional scales. For clustered vegetation, for example, coniferous trees and shrubs, the relation is different; the equation becomes (Huemrich and Goward 1992)

$$L_g = \frac{L_{g,i,\max}\text{FPAR}}{\text{FPAR}_{\max}}. \quad (24)$$

Land-cover classes 4, 5 (needleleaf deciduous and evergreen), and 7 (shrub land, thicket) are treated as clumped vegetation types as defined in Sellers et al. (1992a). In cases where there is a combination of clustered and evenly distributed vegetation, L_g can be calculated by a combination of (23) and (24):

$$L_g = (1 - F_{\text{cl}})L_{g,i,\max} \frac{\log(1 - \text{FPAR})}{\log(1 - \text{FPAR}_{\max})} + F_{\text{cl}} \frac{L_{g,i,\max}\text{FPAR}}{\text{FPAR}_{\max}}, \quad (25)$$

where F_{cl} is the fraction of clumped vegetation in the grid area. The value of F_{cl} is given in Table 3 for each land-cover class.

c. *Canopy greenness fraction N and total leaf area index L_T*

It should be emphasized that the FPAR and green leaf area index values described above refer only to the green portions of the vegetation canopy. It is assumed that a small fraction of the vegetation canopy leaf area index consists of nongreen supportive tissues, the stem-area index L_s (0.076 for forests, 0.05 for grasslands and crops, Table 3). An estimate of the proportion of dead leaves within the canopy is provided by the method originally used by Dorman and Sellers (1989) for SiB1. It is assumed that when a deciduous canopy is growing, all the attached leaves are green. After the maximum leaf area is reached and the canopy starts to lose green leaves, the canopy greenness fraction N is determined by assuming that dead leaves remain within the canopy for one month before falling off or being eaten. Thus, the canopy greenness fraction N is given by

$$N = L_g/L_T, \quad (26)$$

where

$L_T = L_s + L_d + L_g$;
L_d = dead leaf area index
$= L_{g_{n-1}} - L_{g_n}$ and $L_d \geq 0$;
L_g = green leaf area index, from FPAR;
L_T = total leaf-area index;
L_s = stem-area index.

Figure 11 shows FPAR fields for February and August 1987 as calculated by (22). Figure 12 shows L_T fields as produced by Dorman and Sellers (1989) from a survey of the ecological literature as interpreted through SiB1. Figure 13 shows comparable L_T fields derived from the FASIR-NDVI using (25) and (26). Both Figs. 12 and 13 depict data at 4° by 5° resolution as used by the SiB-GCM. Note that these fields are otherwise directly related to the FPAR fields of Fig. 11.

A comparison of Figs. 12 and 13 reveals large differences between the survey-based and satellite-based estimates of L_T. Overall, the original SiB1 values are unrealistically high in the boreal forests and savannas and of course show no spatial variation within natural

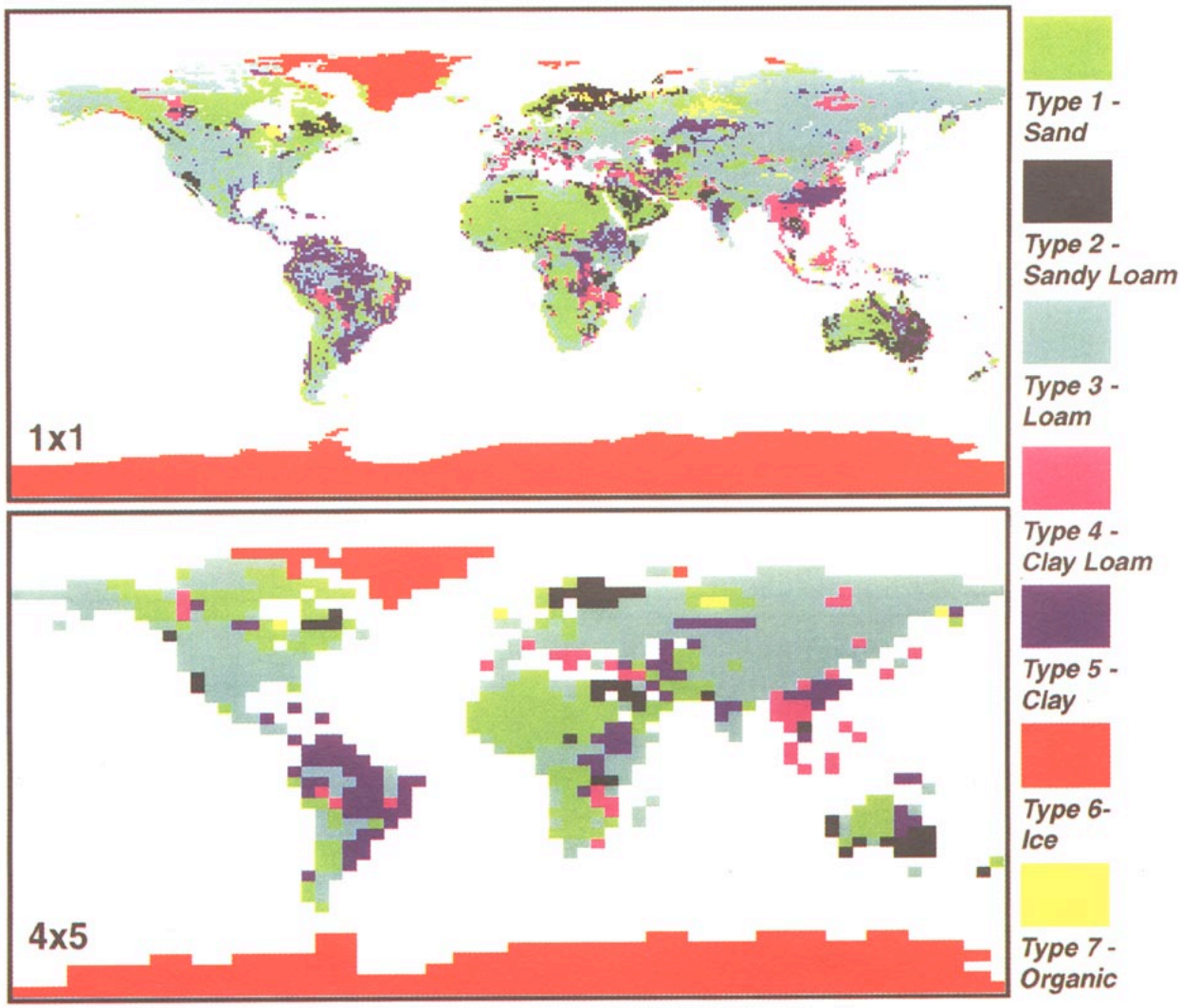

FIG. 15. Soil texture map adapted from Zobler et al. (1986), who processed Food and Agricultural Organization data to create their map. Data are shown at (top) 1° × 1° and (bottom) 4° × 5° resolution. The classes and associated parameters are defined in Table 4.

land-cover classes for any given month (Dorman and Sellers 1989). Interestingly, the SiB2 fields show higher summer L_T values for the seasonal boreal forests of Eastern Siberia and the Great Plains of North America.

Spatially extensive validation datasets corresponding to Figs. 11, 12, and 13 are simply not available. For the time being, we assume that the SiB2 FASIR-NDVI fields are more accurate than equivalent SiB1 fields because of their basis in direct observation and in the theory supporting the satellite-derived product. Detailed validation of these FASIR-NDVI-derived fields must rely on the results of large-scale field experiments, for example, FIFE (Sellers and Hall 1992) and other work and will be the subject of future papers.

6. Generating the global parameter fields from the core datasets

The procedure for making the SiB2-GCM global surface parameter fields consists of combining digital maps (vegetation type and soil type), time series fields (FPAR, L_T, N), and tables of soil and vegetation properties (soil physics by type, vegetation attributes by type, FPAR, L_T, N) to produce a large but self-consistent set of time series fields. Many of these datasets are available at 1° × 1° resolution on CD-ROM; see Meeson et al. (1995). The core source datasets are as follows.

(i) Food and Agricultural Organization/Goddard Institute for Space Studies (FAO/GISS) soil-type

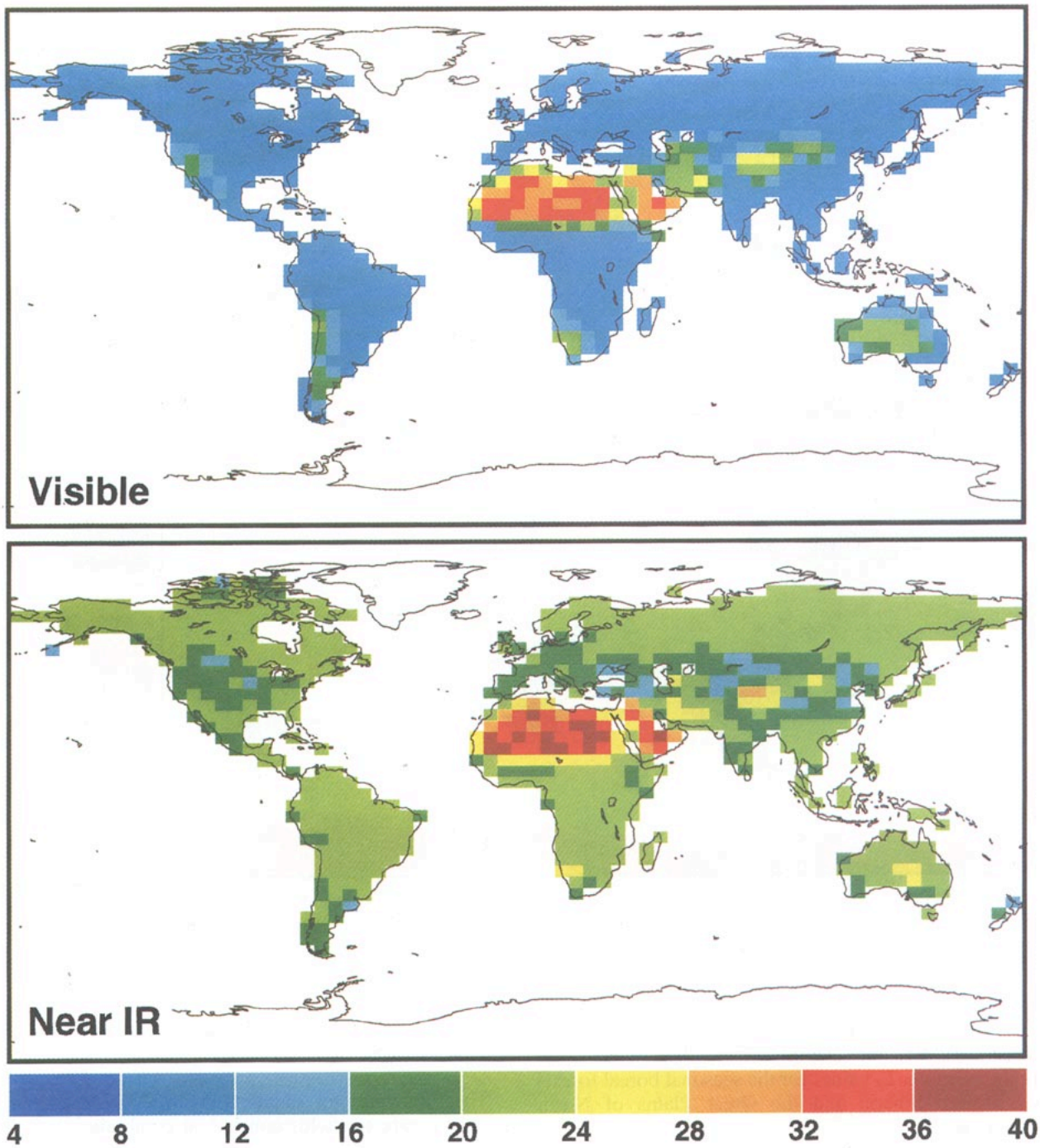

FIG. 16. Snow-free background soil–ground reflectance values in percentages derived from vegetation classification information and ERBE data: (top) visible and (bottom) near-infrared reflectances.

map: this map, derived by Zobler et al. (1986) from analysis of the FAO database, categorizes the world's soils into seven texture classes on a 1° × 1° grid.

(ii) Soil properties table: the texture classes specified in (i) above were applied to a soil physical properties dataset of Clapp and Hornberger (1978) to create a table of soil physics properties (Table 4).

(iii) Earth Radiation Budget Experiment (ERBE) clear-sky surface albedos: the published ERBE (4° by 5°) data of Harrison et al. (1990) were used to "paint" in soil reflectances in desert and semiarid areas (land-

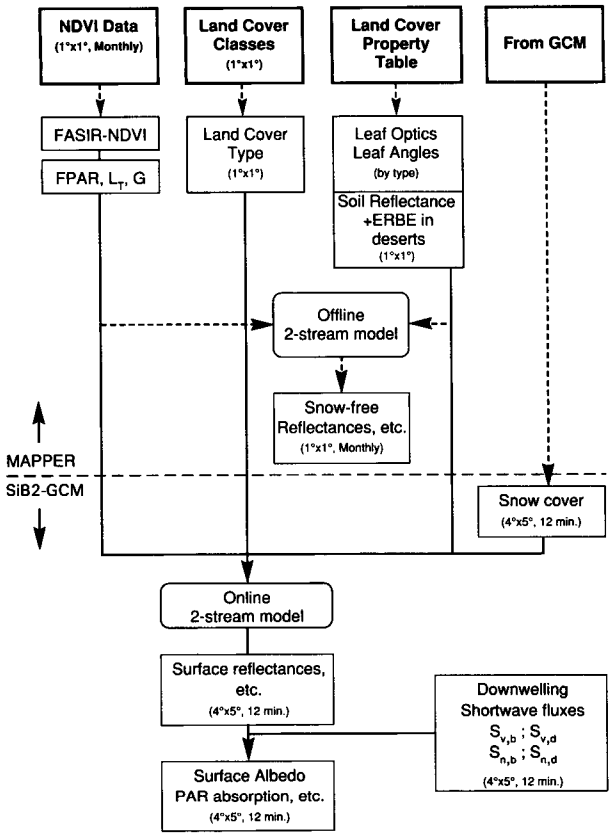

FIG. 17. Schematic of procedures used to generate global surface reflectance and other radiative transfer properties for SiB2. The horizontal dashed line divides off-line preprocessor (MAPPER) tasks from on-line (SiB2-GCM) tasks.

cover types 7 and desert subclasses in type 6 between 45°S and 45°N; see Table 2 and next item).

(iv) Land-cover classes: the land-cover map of Kuchler (1983) as digitized by Willmott (1988, personal communication) and the land-use map of Matthews (1984, 1985) were used by Dorman and Sellers (1989) to produce a 1° by 1° vegetation map for SiB1. The distribution of subtropical and tropical C_4 grasslands (Collatz and Berry 1992, personal communication) and the extent of tropical forest (Nobre et al. 1991) have since been modified to yield a new product, SiB2MAP (see Fig. 5).

(v) Vegetation properties table: each vegetation-type shown on the map of item (iv) above has a set of time-invariant parameters assigned to it (Table 5). The role of each parameter is discussed in Sellers et al. (1996). This table corresponds roughly to Table 1 of Sellers et al. (1986) and Tables 2, 3, and 4 of Dorman and Sellers (1989), except that SiB2 has many fewer parameters (see Table 1 of Sellers et al. 1996). The vegetation properties table is broken into the following categories:

- physical parameters—vegetation morphological and soil depth parameters are assigned in much the same way as in Sellers et al. (1986) and in Dorman and Sellers (1989);
- optical properties—leaf and soil optical properties are assigned as in Dorman and Sellers (1989); note that the grasslands, croplands, and deserts (types 6, 7, 8, 9) share one set of properties, broadleaf forests (1, 2) another, and needleleaf (4, 5) another; the mixed-forest (3) properties are described by the mean of broadleaf and needleleaf properties.
- physiological properties—a broad distinction is made between C_3 ($\epsilon_3 = 0.08$) and C_4 ($\epsilon_4 = 0.05$) vegetation (see Table 5). Other properties, notably the temperature coefficients, vary from type to type. These parameters were obtained from reviews of the ecological literature as partially documented in Collatz et al. (1991, 1992).

(vi) The FASIR-NDVI-derived time series fields of FPAR, L_T, and N. These have been described in the previous two sections.

The next four subsections describe how these datasets are combined using simple relational rules or through intermediate models to produce the land surface parameter fields for SiB2. This task is performed by a series of subroutines in an off-line preprocessor for SiB2 called MAPPER (Figs. 14, 15, 16, and 17). The resulting fields, shown in Table 6, are accessed directly by SiB2 from within the GCM. Generally speaking, the 1° by 1° cells are averaged up to 4° by 5° monthly fields and linear temporal interpolation is used to define the daily value of each parameter between the fifteenth day of each month. No direct use of the land cover or soil maps is made from within the GCM since the accessed fields consist of those properties that are directly used in SiB2 and/or GCM calculations, for example, roughness length, reflectance, FPAR, etc.

a. Soil physical properties and reflectance properties

Figure 14 outlines the procedure for producing the global soil properties fields. The soil-type map (Fig. 15) and soil properties table are combined to produce fields of the textural parameters: θ_s, B, K_s, and Ψ_s. The land-cover map and the vegetation-type-dependent properties of soil depths and slopes are combined to create global fields of these parameters. The depth of the topmost layer is always 0.02 m (D_1); the root zone layer thickness D_2 is defined as $D_2 = D_r - D_1$; the recharge zone layer thickness D_3 is defined as $D_3 = D_T - D_r$, where D_r is the root depth and D_T is the total depth of the hydrologic active soil layer. Soil or litter background reflectances (visible and NIR) are important parameters for calculating the albedo of sparsely

TABLE 6. Parameter fields used by SiB2 within the GCM. In the application described in Randall et al. (1996) all of the above parameters are defined as global fields generated from the datasets described in section 6.

Static parameters associated with land-cover class		
Z2	z_2:	Canopy-top height (m)
Z1	z_1:	Canopy-base height (m)
VCOVER	V:	Vegetation-cover fraction
CHIL	χ_L:	Leaf-angle distribution factor
SODEP	D_T:	Total depth of three soil moisture layers (m)
ROOTD	D_r:	Rooting depth (m)
TRAN	$\delta_{v,N}$:	Leaf transmittance
REF	$\alpha_{v,N}$:	Leaf reflectance
SOREF	$\alpha_{s,v,N}$:	soil reflectance
VMAX0	$V_{\max,0}$:	Rubisco velocity of sun leaf (mol m^{-2} s^{-1})
EFFCON	ϵ:	Quantum efficiency (mol mol^{-1})
GRADM	m:	Conductance–photosynthesis slope parameter (mol m^{-2} s^{-1})
BINTER	b:	Conductance–photosynthesis intercept (mol m^{-2} s^{-1})
ATHETA	β_{ce}:	w_c, w_e coupling parameter
BTHETA	β_{ps}:	w_p, w_s coupling parameter
TRDA	s_5:	Slope of high temperature inhibition function (leaf respiration, K^{-1})
TRDM	s_6:	One-half point of high temperature inhibition function (leaf respiration, K)
TROP	298:	Temperature coefficient in GS-A model (K)
PHC	Ψ_c:	One-half critical leaf-water potential limit (m)
RESPCP	f_d:	Respiration fraction of $V_{\max}$
SLTI	s_3:	Slope of low temperature inhibition function (K^{-1})
HLTI	s_4:	One-half point of low temperature inhibition function (K)
SHTI	s_1:	Slope of high temperature inhibition function (K^{-1})
HHTI	s_2:	One-half point of high temperature inhibition function (K)
Static parameters associated with soil type		
BEE	B:	Soil wetness exponent
PHSAT	Ψ_s:	Soil tension at saturation (m)
SATCO	K_s:	Hydraulic conductivity at saturation (m s^{-1})
POROS	θ_s:	Soil porosity (volume fraction)
SLOPE	$\varnothing_s$:	Mean topographic slope (rad)
Time–space-varying vegetation parameters from SVI		
APARC	FPAR:	Canopy absorbed fraction of PAR
ZLT	L_T:	Leaf area index
GREEN	N:	Canopy greenness fraction
Parameters derived from the above		
Z0D	z_0:	Roughness length (m)
DD	d:	Zero plane displacement (m)
CC1	C_1:	Bulk boundary resistance coefficient [$(s\ m^{-1})^{1/2}$]
CC2	C_2:	Ground to canopy air-space resistance coefficient
GMUDMU	$G(\mu)/\mu$:	Time–mean leaf projection

vegetated areas. As a default, the vegetation-type-dependent values of soil background reflectance are used to create global fields. In comparisons with ERBE data, this procedure was found to give unrepresentative albedos for the deserts of Australia and Northwest America, which had been assigned soil reflectance values typical of the Sahara. To remedy this, the ERBE data of Harrison et al. (1990) were used to paint in the desert areas (type 7 and desert subclasses in 6 between 45°S and 45°N) (see Fig. 16). The amalgamated soil properties maps at 1° by 1° are accessed directly by the MAPPER preprocessor of SiB2 without intermediate reference to the soils or land-cover maps.

b. Radiative transfer properties

The canopy greenness fields (N) from the FASIR-NDVI product are used with the land-cover map and leaf optical properties to create weighted (by live–dead fraction) leaf optical properties for each grid area. These fields, plus the soil–litter reflectance fields (previous section), can be used in an off-line version of the two-stream model of Sellers (1985) to calculate monthly 1° × 1° fields of snow-free reflectances. However, these are not accessed by SiB2 from within the GCM. Instead, the soil and leaf optical properties are modified in the presence of snow (Sellers et al. 1995) and a vectorized version of the two-stream model called from within the GCM is used to calculate the actual time- and space-varying surface reflectances. The GCM also supplies fields of the incident shortwave radiation fluxes (visible, NIR, direct beam, and diffuse) every time step. These are combined with the reflectance fields and some other derived surface properties to calculate albedos and the fractions of the incident radiation fluxes absorbed by the canopy and soil (see Fig. 17 and Sellers et al. 1996). Figure 18 shows snow-free albedo fields produced by the off-line model. Examples of SiB2 albedo fields that include the effects of snow may be found in Randall et al. (1996).

c. Turbulent transfer properties

The first-order closure model of Sellers et al. (1989, 1996) is applied off-line to the vegetation properties subset of morphological parameters (z_2, z_c, z_1, z_s, l_w, l_l, χ_L; see Table 5 for definitions) to create look-up tables for each vegetation type of the bulk aerodynamic parameters of roughness length (z_0), zero plane displacement (d), canopy boundary-layer transfer parameter (C_1), and soil to canopy air-space parameter (C_2). The model is cycled to produce values of these bulk parameters for each vegetation type for leaf area indices ranging from 0 to 8.0 in 0.5 increments. This look-up table (SIBAERO) is combined with the L_T fields and land-cover map to produce 1° by 1° monthly snow-free fields of z_0, d, C_1, and C_2. Linear interpolation is used between the look-up table values to provide estimates of these parameters for each grid area and month.

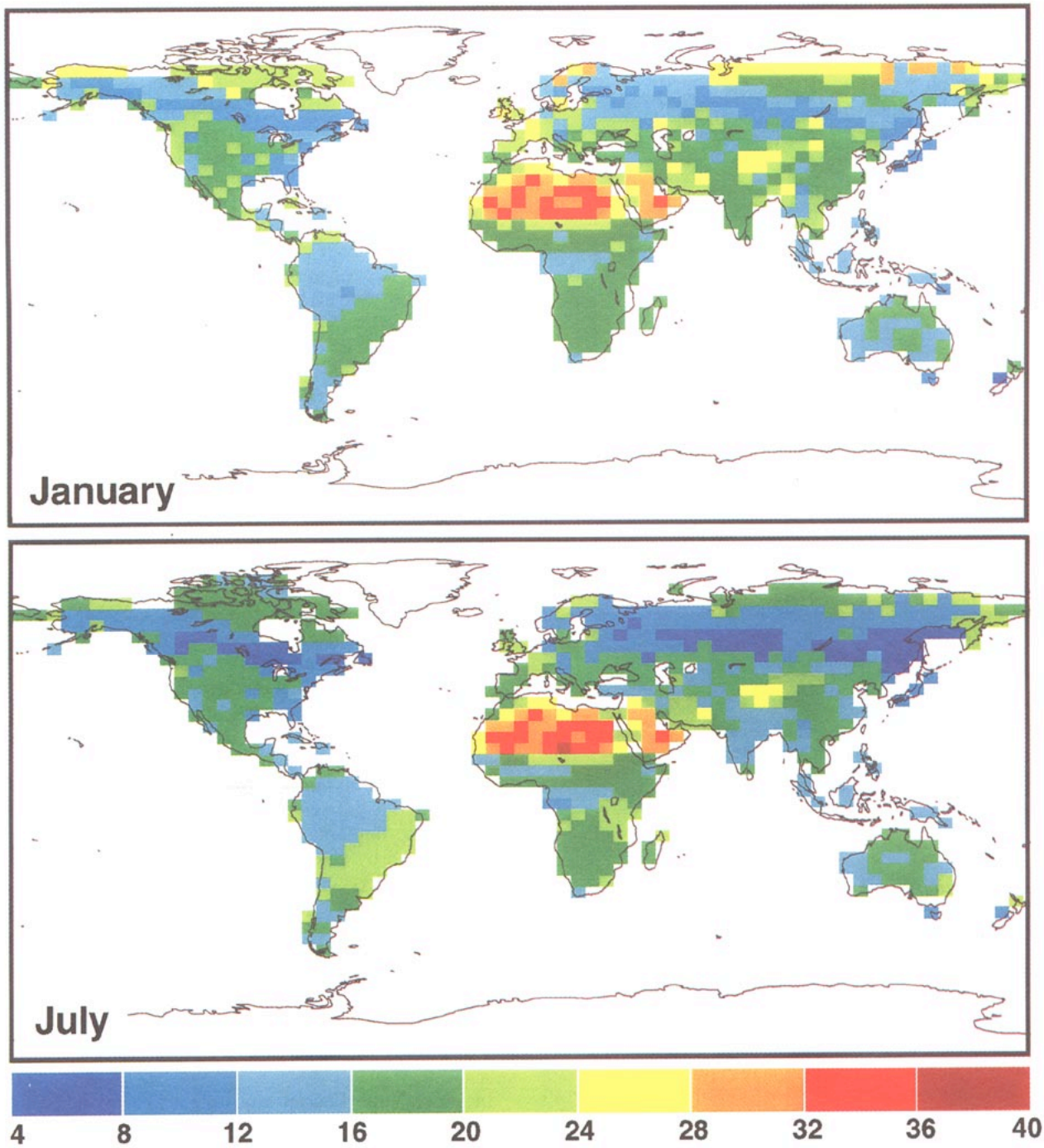

FIG. 18. (top) January and (bottom) July snow-free clear-sky albedos in percentages produced by an off-line SiB2 calculation following the procedure shown in Fig. 16.

In the GCM, SiB2 accesses these snow-free fields and adjusts them for the effect of snow accumulation at every time step. These adjusted values are then used by the nonneutral turbulent transfer submodel of SiB2 to calculate r_a, r_b, and r_d each time step (Fig. 19 and Sellers et al. 1995). Figure 20 shows snow-free roughness lengths calculated by SiB2.

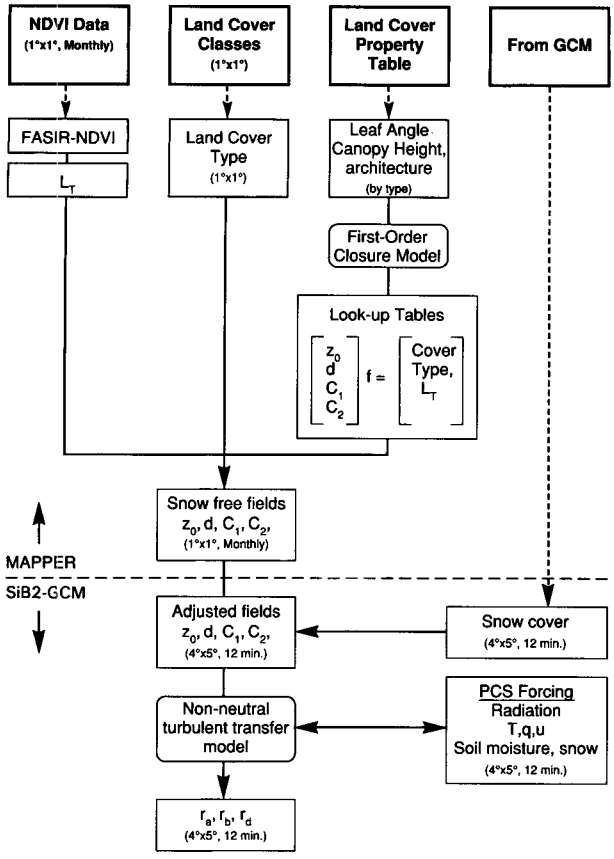

FIG. 19. Schematic of procedures used to generate global fields of turbulent transfer properties for SiB2. The horizontal dashed line divides off-line preprocessor (MAPPER) tasks from on-line (SiB2-GCM) tasks. PCS stands for physical climate system, other symbols are defined in Table 5.

d. Vegetation biophysical parameters

Vegetation-type and some associated parameters ($L_{T,\max}$, $\mathrm{SR}_{\max}$, $\mathrm{SR}_{\min}$) have already been used in the calculation of FPAR, L_T, and N from the FASIR-NDVI fields. An off-line calculation of mean monthly solar (radiation-weighted) angle is used in conjunction with the vegetation properties (optical and leaf angle characteristics) to calculate the 1° by 1° monthly time-mean, radiation-weighted values of the PAR extinction coefficient $\bar{k}$. The canopy PAR-use parameter Π is then calculated from $\Pi \approx \mathrm{FPAR}/\bar{k}$ (Sellers et al. 1992a, 1995). Where Π is combined with other surface parameters in SiB2 to calculate A_c and g_c and from these, the fluxes of radiation, heat, mass (CO_2 and H_2O), and momentum (Fig. 21; Sellers et al. 1996). Figure 22 shows values of Π calculated by SiB2.

7. Discussion

Significant changes were made in the SiB2 land-surface parameterization with respect to the previous SiB1 version. Most importantly, vegetation-related parameters for the land surface were directly derived from satellite observations, that is, the 1° × 1° NDVI dataset discussed by Los et al. (1994), rather than inferred from ground-cover classes. For the calculation of the vegetation-related parameter fields, two major issues had to be addressed: inconsistencies in the source NDVI data had to be accounted for, and relationships between the NDVI and the land-surface parameters had to be established. Correction of the NDVI was hampered by the absence of component channel 1 and 2 data and the lack of information on viewing geometry in the source global dataset. Adjustment procedures were developed based on some assumptions about the properties of NDVI datasets associated with different land-cover classes. Some of these assumptions, such as the supposition that most of the major sources of error tend to lower the value of the NDVI, have been largely validated by research and can be used with a high level of confidence (e.g., Holben 1986; Los et al. 1994). Other assumptions have not been as thoroughly investigated.

The NDVI data were adjusted with a series of corrections, collectively referred to as FASIR (Fourier-adjustment, solar zenith angle correction, interpolation, and reconstruction). These corrections were applied in a predefined sequence, such that corrections less dependent on additional non-NDVI data sources were applied first, and corrections that depended more heavily on additional data used were applied last. Specifically, the Fourier-adjustment uses only the NDVI data and does not require input from an additional data source. For the solar zenith angle correction a land-cover classification and estimates of solar zenith angle are used, however, the outcome of the calculations is not seriously affected by changes in the classification; the interpolation and reconstruction were done specifically for GCM purposes and depend heavily on the land-cover classification.

Figure 23 shows the effect of each of the FASIR corrections by latitude band for July. The average by latitude band of the NOAA-GVI (Tarpley et al. 1994) is also shown for comparison. Figure 24 shows the effect of the FASIR corrections by biome for the entire year.

In general, the Fourier-adjustment (FA of FASIR) provides a conservative correction to the data, that is, suspect values are adjusted relative to the position of more reliable data. The procedure may lead to some small overestimations in specific cases, for example, when a large, sudden change in the amount of vegetation occurs, such as in climates with large seasonality. For these biomes, overestimation could be a problem at the start and end of the growing season. Figures 23 and 24 indicate that the FA correction is most significant for biomes with a large fraction of dense, green vegetation cover, where the impacts of cloud contamination and atmospheric water vapor are expected to be

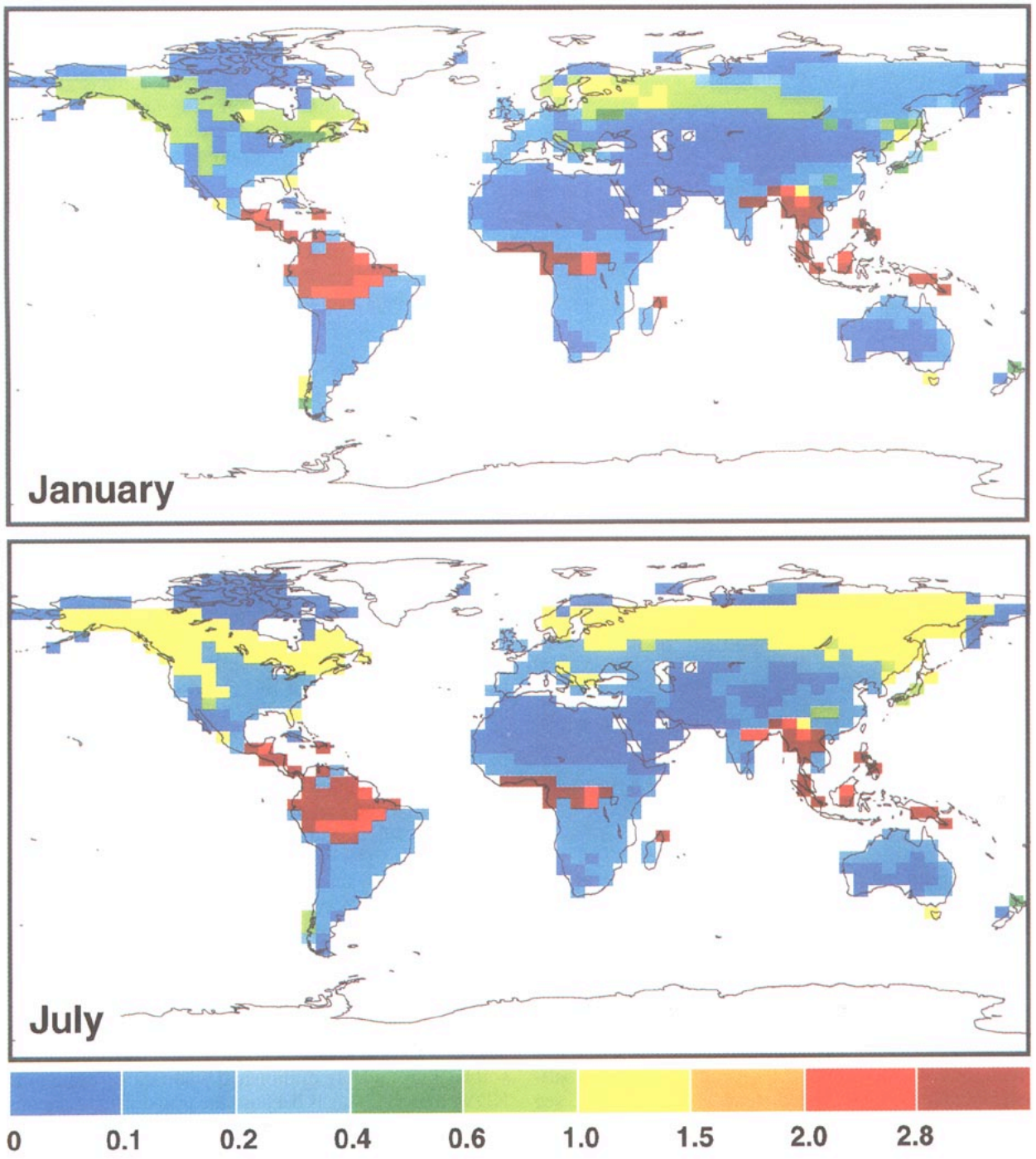

FIG. 20. (top) January and (bottom) July snow-free roughness lengths (m) produced by SiB2.

strongest. The correction can also be significant for biomes with large seasonality, indicating that an overestimate during the start and end of the growing season is possible. The Fourier-adjustment has a marginal effect over deserts and an intermediate effect for grasslands, needleleaf deciduous, shrublands, and tundra. Because the Fourier-adjustment has the greatest effect on areas where NDVI time series are expected to be most suspect, it is assumed that the improvements provided by this procedure outweigh its disadvantages. For photosynthesis calculations in SiB2-GCM, overestimates in the NDVI at the start and end of the growing

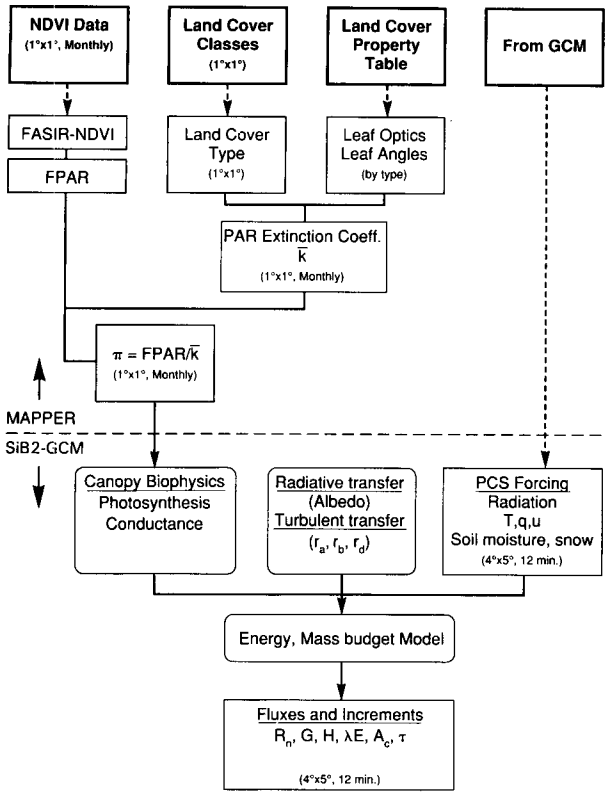

FIG. 21. Schematic of procedures used to generate global fields of surface biophysical properties for SiB2, principally the canopy PAR-use parameter, Π. The horizontal dashed line divides off-line preprocessor (MAPPER) tasks from on-line (SiB2-GCM) tasks. Also shown are the connections with other SiB2 submodels to calculate the surface fluxes and hence the increments in the SiB2 and atmospheric boundary layer prognostic variables (Sellers et al. 1996).

season should have only a minor impact because ambient temperatures are low and will counteract possible overestimates in assimilation rates.

The solar zenith angle adjustment (S of FASIR) incorporates a number of assumptions that have yet to be validated against in situ observations. The effect of this correction is greatest for vegetation types at high latitudes–solar zenith angles (tundra, needleleaf evergreen, and deciduous) and temperate regions (broadleaf deciduous, mixed needleleaf, and deciduous; see Fig. 24). The solar zenith angle correction is more conservative than the one derived from first principles by Singh (1988) (Fig. 8). Although there is some uncertainty about this correction, overall it should improve the data and it is likely that any overcorrections are small. View angle effects in the source 1° by 1° NDVI data are expected to be small: the compositing technique favors selection of maximum NDVI values that should be grouped around an average view angle of 10° in the off-nadir forward-scatter direction. Viewangle effects in the NDVI are relatively small at and around this view direction. Remnants of view angle effects in the 1° by 1° data are confounded with and partially accounted for by the solar zenith angle correction: the correction is derived from the dataset itself, and thus should partially correct for systematic higher or lower deviations due to biases in viewing angle when confounded with solar angle. Residual variations in the NDVI as a result of unconfounded variations in view angle are not accounted for.

The interpolation (I in FASIR) of missing data for the Northern Hemisphere evergreen needleleaf vegetation in winter is necessary to obtain realistic estimates of several land surface parameters in SiB2, in particular those derived from the leaf area index fields such as albedo and roughness length. Failure to provide NDVI estimates for the winter period would effectively set the leaf area index values to zero and result in near-zero roughness lengths and high albedos. This would remove the effects of the boreal forests on the physical climate system during winter. For lack of an alternative, a best guess of the minimum NDVI value is made by selecting the value at the end of the growing season before any snowfall is likely to have occurred. Overestimation of the NDVI for these higher latitudes outside the growing season is unlikely to lead to excessive evapotranspiration or assimilation rates in SiB2 because of the low ambient temperatures.

The reconstruction (R in FASIR) of NDVI time series for the tropical evergreen broadleaf vegetation is necessary to correct for the effect of persistent cloud cover and atmospheric water vapor effects associated with tropical forests. Low NDVI values would result in low FPAR and leaf area index estimates. A side effect of the procedure is that all seasonality in the data is eliminated and that areas incorrectly classified as evergreen broadleaf will have high NDVI values throughout the year. The procedure does provide an overall improvement in that it diminishes the number of outliers, especially in very cloudy areas. We have no real alternative approach until higher resolution, multiyear datasets become available in which cloud-contaminated data can be identified and discarded and water vapor corrections applied.

Errors at the low end of the NDVI, for example, as a result of variations in the reflective properties of the soil background, are diminished when transforming the NDVI into SR. This is because the transformation tends to compress the lower values of the NDVI, whereas the higher values become stretched. Errors in the NDVI at the low end will therefore have little impact on SR and hence FPAR values.

Relationships between the NDVI and biophysical parameters have been established mainly from in situ studies involving individual plant species and high-resolution radiometric data. Recently, a number of studies have focused on the extrapolation of the relationship between FPAR and SR from the plot scale (a few meters) to intermediate spatial scales on the order of 100 m^2 to 15 km^2 (Sellers et al. 1992b). The results support

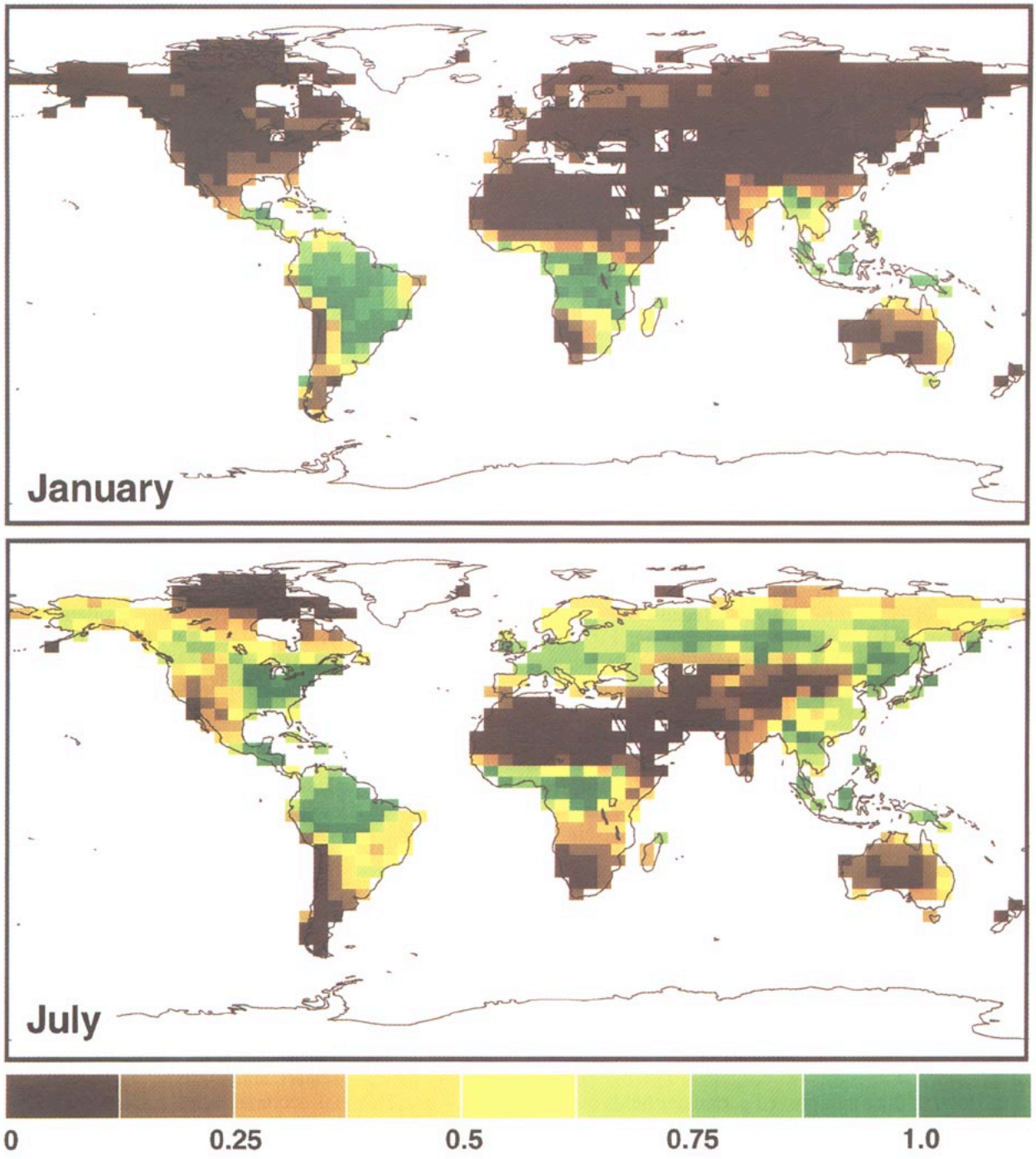

FIG. 22. (top) January and (bottom) July fields of the canopy PAR-use parameter Π produced by SiB2.

a near-linear relationship between SR and biophysical properties and, by inference FPAR, over this range of spatial scales (Hall et al. 1992). The near-linear properties of the SR–FPAR relationship, combined with assumptions on the occurrence of minimum and maximum vegetation activity, has encouraged us to calculate global fields of FPAR; total leaf area index L_T; and canopy greenness fraction N from the satellite data. It is doubtful that the near-linearity of the FPAR-SR relationship holds for all land-cover classes and soil backgrounds; it has been suggested that for some cases, for example, bright soil backgrounds, the relation be-

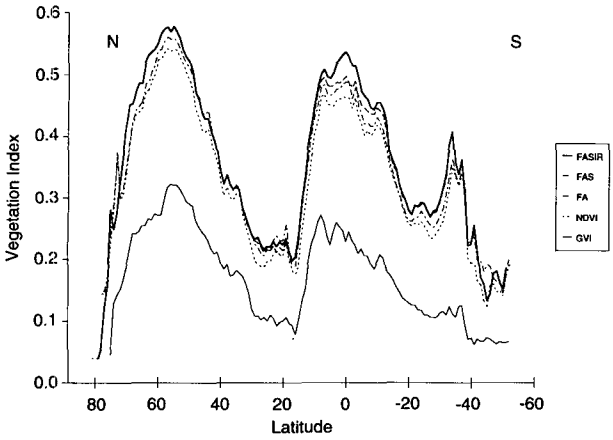

FIG. 23. Effect of Fourier-wave adjustment, solar zenith angle correction, interpolation, and reconstruction on the global NDVI averaged by latitude for the month of July 1987. The GVI product (Tarpley et al. 1984) is shown for comparison. Averages for each of the products are calculated with missing values set to NDVI (or GVI) set to zero, see text for discussion.

tween FPAR and NDVI may be more linear than the relationship between FPAR and SR (Choudhury 1987; Goward and Huemmrich 1992). Because of the dark soil background assumption, we expect our FPAR estimates to be less reliable for intermediate NDVI values over areas with a bright soil background. For high and low NDVI values we still expect our estimates to be reasonable since the effect of nonlinearities should be small close to the end-points to which the SR-FPAR relationship was tied. Because FPAR is critical to calculations of vegetation activity, further research is needed to establish a more accurate relationship between FPAR and vegetation indices.

We have more confidence in the estimates of FPAR than L_T. However, we have seen that the essential surface properties are near-linearly related to FPAR rather than L_T, which is only used as an intermediate variable. Therefore, our uncertainties in albedo, surface roughness, canopy conductance, and photosynthesis seem to scale directly with the errors in the NDVI (SR) and FPAR rather than with the errors in the estimation of L_T.

In order to obtain improved parameter fields over the ones described in this paper, a number of items need to be addressed. In the first place, the source satellite dataset could be improved by the incorporation of individual channel data that are corrected for scattering by atmospheric aerosols and molecules, absorption by atmospheric water vapor and ozone, cloud contamination, and off-nadir viewing and solar zenith angle geometry. Studies are underway to obtain an improved spectral vegetation dataset in which many of these problems are addressed. Further improvements could be expected from future remote sensing devices, such as the moderate-resolution imaging spectroradiometer that are designed specifically to address vegetation monitoring. Second, procedures for deriving biophysical parameter fields from the NDVI could also be improved. The results from algorithm development studies reported in Sellers and Hall (1992) could be taken further, particularly by addressing variations due to different vegetation types and soil backgrounds. A third area in which improvements can made is in the stratification of vegetation types. A classification based on satellite-derived biophysical parameters, for example, surface reflectance and FPAR, rather than on a set of inconsistently specified land-cover classes, is greatly preferred.

Although the FASIR-NDVI and the relationships used to derive global fields of FPAR and L_T have serious limitations, much has been gained over previous attempts to specify global surface parameter fields (e.g., Dorman and Sellers 1989). Most important, it has become possible to address realistically the spatial and temporal variability of land-surface parameters within a climate model.

The NOAA global vegetation index (GVI) dataset (Tarpley et al. 1984) was considered as an alternative data source for this work but was thought to be less suitable for our purposes, despite the availability of component channel data retained with the GVI composites. As described by Gutman (1991), the GVI data tend to be lower than the NDVI because 1) they are not normalized for incoming solar radiation in the respective bands, and 2) the GVI compositing technique has a strong bias toward selecting data from the extreme backscatter direction (40°–50° off-nadir). Figure 23 shows a comparison of the global zonal averages of the GVI, NDVI, and FASIR-NDVI data for the month of July 1987. The GVI values are lower overall because the component channel values were not normalized for the solar flux in the visible and near-infrared bands. In addition, the GVI and NDVI differ significantly at latitudes below 20°S, although to a lesser extent an overall discrepancy in signature can be found in the entire Southern Hemisphere. The difference in signal here is most likely explained by the different viewing angles associated with the NDVI and GVI, that is, near forward-scatter and extreme backscatter, respectively. This bias becomes more significant for large solar zenith angles, up to a point where the entire signal from the land surface is lost, both in the GVI as well as in its concurrent channel 1 and 2 data. Goward et al. (1994) therefore assign GVI data from solar zenith angles larger than 70° as spurious; however, it is likely that GVI data collected at much smaller solar zenith angles are affected as well.

8. Conclusions

The revised Simple Biosphere model, SiB2, of Sellers et al. (1996) has a far smaller core set of parameters

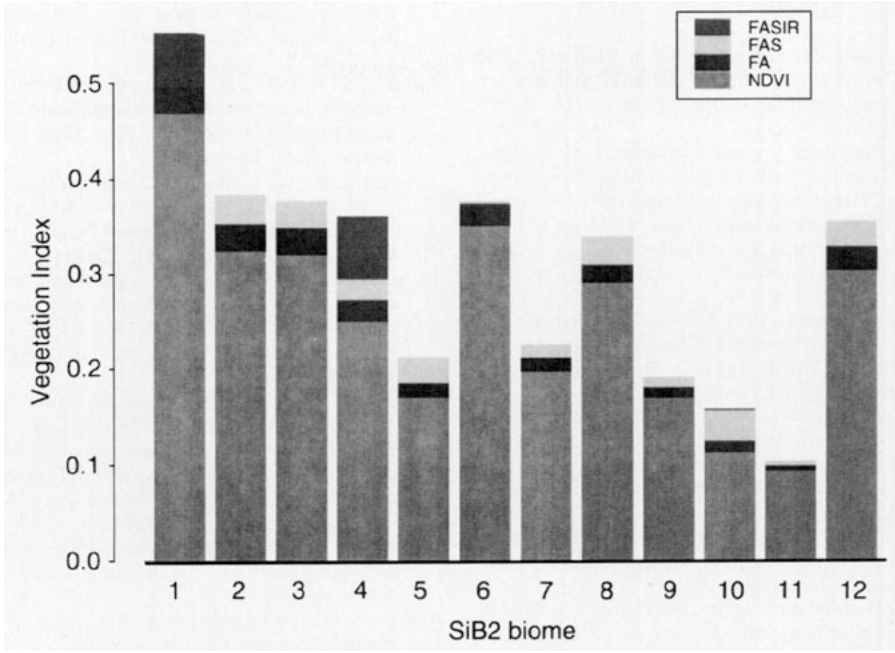

FIG. 24. Average NDVI values by biome for the entire year of 1987 with the subsequent FASIR corrections (Fourier-wave adjustment, solar zenith angle correction, interpolation, and reconstruction) shown for comparison. Missing values were set to zero prior to averaging.

than the original SiB1 of Sellers et al. (1986). This is due to some simplification—reduction to a single layer of vegetation and incorporation of a much simpler soil moisture stress model—and the use of a more realistic and universal formulation to describe canopy conductance and photosynthesis. Photosynthesis was not calculated in SiB1 at all. In SiB1, the phenologically varying vegetation properties (L_T and N) were prescribed by vegetation type and month; in the case of croplands, a complex procedure was used to describe their seasonal and latitudinal variations (Dorman and Sellers 1989). In SiB2 all of the time and space variations in L_T, N, and FPAR are calculated from the satellite dataset. In summary, the SiB2 dataset has the following benefits over that of SiB1 as written up in Dorman and Sellers (1989):

(i) realistic time–space variations in FPAR, L_T, and N;
(ii) realistic time–space variations in products derived from FPAR, L_T, and N, principally the surface reflectances, surface turbulent transfer characteristics (z_0, d, C_1, C_2), and surface biophysical parameters;
(iii) improved soil reflectance fields, partially derived from ERBE data—this yields better albedo fields in the worlds desert and arid zones;
(iv) improved soil physical properties fields—global soil texture information is used rather than assigning soil properties by land-cover type;
(v) direct use of parameter fields—in SiB1, parameters were accessed through vegetation type. In SiB2, parameter fields are generated off-line and accessed directly from within the GCM. This will allow averaging of properties within the GCM grids from the original 1° by 1° data in future work and leaves the way open for using finer-resolution datasets if necessary.

Finally, a note on the effects of uncertainties in the FASIR-NDVI data on the accuracy of the parameter fields as used in SiB2. It was shown in previous sections that errors or uncertainties in the NDVI will translate approximately linearly into errors or uncertainties in FPAR, reflectance, conductance, photosynthesis, and thus evapotranspiration. However, the errors in leaf area index L_T are likely to be proportionally far worse due to the generally exponential dependence of green leaf area index (NL_T) on FPAR. In a sense, this does not matter too much, as canopy reflectance, transpiration, and photosynthesis appear to be near-linearly related to FPAR and the Simple Ratio vegetation index (a transform of the NDVI) and only secondarily and nonlinearly on leaf area index.

Acknowledgments. This work was funded by a NASA Earth Observing System—Interdisciplinary Science grant (Sellers–Mooney). David Strauss of COLA, Department of Meteorology of the University of Maryland is thanked for his advice on Fourier series. The members of the GIMMS group at NASA Goddard Space Flight Center are thanked for their assistance in data processing. Dr. Asrar of NASA HQ is thanked for arranging funding support and for his encouragement. Drs. Williams, Schnetzles, and Kerber of NASA/GSFC are thanked for accommodation arrangements.

REFERENCES

Asrar, G., M. Fuchs, E. T. Kanemasu, and J. L. Hatfield, 1984: Estimating absorbed photosynthetic radiation and leaf area index from spectral reflectance in wheat. *Agron. J.*, **76,** 300–306.

Ball, J. T., 1988: An analysis of stomatal conductance. Ph.D. thesis, Department of Biological Sciences, Stanford University, 89 pp.

Budyko, M. I., 1974: *Climate and Life.* Academic Press, 508 pp.

Choudhury, B. J., 1987: Relationships between vegetation indices, radiation, absorption and net photosynthesis evaluated by a sensitivity analysis. *Remote Sens. Environ.*, **22,** 209–233.

Clapp, R. B., and G. M. Hornberger, 1978: Empirical equations for some soil hydraulic properties. *Water Resour. Res.*, **14.4,** 601–604.

Collatz, G. J., J. T. Ball, C. Grivet, and J. A. Berry, 1991: Physiological and environmental regulation of stomatal conductance, photosynthesis, and transpiration: A model that includes a laminar boundary layer. *Agric. For. Meteor.*, **54,** 107–136.

——, M. Ribas-Carbo, and J. A. Berry, 1992: Coupled photosynthesis stomatal conductance model for leaves of C_4 plants. *Aust. J. Plant Physiol.*, **19,** 519–538.

Deering, D. W., T. F. Eck, and T. Grier, 1992: Shinnery oak bidirectional reflectance properties and canopy model inversion. *IEEE Trans. Geosci. Remote Sens.*, **30,** 339–348.

Dickinson, R. E., 1984: Modeling evapotranspiration for three-dimensional global climate models. *Climate Processes and Climate Sensitivity, Geophysical Monogr.*, No. 29, J. E. Hansen and T. Takahashi, Eds., Amer. Geophys. Union, 58–72.

Dorman, J. L., and P. J. Sellers, 1989: A Global climatology of albedo, roughness length, and stomatal resistance for atmospheric general circulation models as represented by the simple biosphere model (SiB). *J. Appl. Meteor.*, **28,** 833–855.

Eck, T. F., and V. L. Kalb, 1991: Cloud screening for Africa using geographically and seasonally variable infrared threshold. *Int. J. Remote Sens.*, **12,** 1205–1221.

Farqhuar, G. D., S. Von Caemmerer, and J. A. Berry, 1980: A biochemical model of photosynthetic CO_2 fixation in leaves of C_3 species. *Planta,* **149,** 78–90.

Goward, S. N., and K. F. Huemmrich, 1992: Vegetation canopy PAR absorptance and the normalized difference vegetation index: An assessment using the SAIL model. *Remote Sens. Environ.*, **39,** 119–140.

——, S. Turner, D. Dye, and S. Liang, 1994: The University of Maryland improved global vegetation index product. *Int. J. Remote Sens.*, **15,** 3365–3395.

Gutman, G. G., 1991: Vegetation indices from AVHRR: An update and future prospects. *Remote Sens. Environ.*, **35,** 121–136.

Hall, F. G., K. F. Huemmrich, and S. N. Goward, 1990: Use of narrow-band spectra to estimate the fraction of absorbed photosynthetically active radiation. *Remote Sens. Environ.*, **32,** 47–54.

——, ——, S. J. Goetz, P. J. Sellers, and J. E. Nickeson, 1992: Satellite remote sensing of surface energy balance: Success, failures and unresolved issues in FIFE. *J. Geophys. Res.*, **97,** 19 061–19 089.

Harrison, E. F., P. Minnis, B. R. Barkstrom, V. Ramanathan, R. D. Cess, and G. G. Gibbson, 1990: Seasonal variation of cloud radiative forcing derived from the Earth Radiation Budget Experiment. *J. Geophys. Res.*, **95,** 18 687–18 703.

Hoaglin, D. C., F. Mosteller, and J. W. Tukey, 1983: *Understanding Robust and Exploratory Data Analysis.* Wiley, 447 pp.

Holben, B. N., 1986: Characteristics of maximum-value composite images for temporal AVHRR data. *Int. J. Remote Sens.*, **7,** 1435–1445.

——, D. Kimes, and R. S. Fraser, 1986: Directional reflectance response in AVHRR red and near-IR bands for three cover types and varying atmospheric conditions. *Remote Sens. Environ.*, **19,** 213–236.

Huemmrich, K. F., and S. N. Goward, 1992: Spectral vegetation indexes and the remote sensing of biophysical parameters. *Proc. Int. Geosci. Remote Sens. Symp. (IGARSS).* Houston, TX, Institute of Electrical and Electronics Engineers, 1017–1019.

Justice, C. O., T. F. Eck, D. Tanré, and B. N. Holben, 1991: The effect of water vapor on the normalized difference vegetation index for the Sahelian region from NOAA-AVHRR data. *Int. J. Remote Sens.*, **12,** 1165–1187.

Kidwell, K. B., 1991: NOAA polar orbiter data (TIROS-N, NOAA-6, NOAA-7, NOAA-8, NOAA-9, NOAA-10, NOAA-11 and NOAA-12) users guide. National Oceanic and Atmospheric Administration, Washington D.C., 295 pp.

Kimes, D. S., 1983: Dynamics of directional reflectance factor distributions for vegetation canopies. *Appl. Opt.*, **22,** 1364–1372.

Klink, K., and C. J. Wilmott, 1985: Notes on a global vegetation data set for use in GCMs. Department of Geography, University of Delaware, 83 pp.

Kuchler, A. W., 1983: World map of natural vegetation. *Goode's World Atlas,* 16th ed., Rand McNally, 16–17.

Los, S. O., 1993: Calibration adjustment of the NOAA AVHRR normalized difference vegetation index without recourse to component channel 1 and 2 data. *Int. J. Remote Sens.*, **14,** 1907–1917.

——, C. O. Justice, and C. J. Tucker, 1994: A 1° by 1° global NDVI data set for climate studies calculated from the GIMMS continental NDVI data. *Int. J. Remote Sens.*, **15,** 3493–3518.

Matthews, E., 1983: Global vegetation and land use: New high-resolution data bases for climate studies. *J. Climate Appl. Meteor.*, **22,** 474–487.

——, 1984: Prescription of land-surface boundary conditions in GISS GCM II: A simple method based on high resolution vegetation data bases. NASA Tech. Memo. 86096, NASA, Washington D.C. 20 pp.

——, 1985: Atlas of archived vegetation, land-use and seasonal albedo data sets. NASA Tech. Memo. 86199, NASA, Washington D.C. 53 pp.

Meeson, B. W., F. E. Corprew, D. M. Myers, J. W. Closs, K.-J. Sun, and P. J. Sellers, 1995: ISLSCP Initiative I—Global Data Sets for Land-Atmosphere Models, 1987–1988. Vol. 1–5. CD-ROM. NASA, (USA NASA GDAC ISLSCP-001 USA NASA GDAAC ILSCP 005).

Monteith, J. L., and M. H. Unsworth, 1990: *Principles of Environmental Physics.* Edward Arnold, 291 pp.

Myneni, R. B., G. Asrar, D. Tanré, and B. J. Choudhury, 1992: Remote sensing of solar radiation absorbed and reflected by vegetated land surface. *IEEE Trans. Geosci. Remote Sens.*, **30,** (2), 302–314.

Nobre, C. A., P. J. Sellers, and J. Shukla, 1991: Amazonian deforestation and regional climate change. *J. Climate,* **4,** 957–988.

Price, J. C., 1991: Timing of NOAA afternoon passes. *Int. J. Remote Sens.*, **12,** 193–198.

Randall, D. A., P. J. Sellers, J. A. Berry, D. A. Dazlich, C. Zhang, J. A. Collatz, A. S. Denning, S. O. Los, C. B. Field, I. Fung, C. O. Justice, and C. J. Tucker, 1996: A Revised land-surface parameterization (SiB2) for GCMs. Part III: The greening of the Colorado State University General Circulation Model. *J. Climate,* **9,** 738–763.

Sato, N., P. J. Sellers, D. A. Randall, E. K. Schneider, J. Shukla, J. L. Kinter, Y-T. Hou, and E. Albertazzi, 1989: Effects of implementing the simple biosphere model (SiB) in a general circulation model. *J. Atmos. Sci.*, **46,** 2757–2782.

Sellers, P. J., 1985: Canopy reflectance, photosynthesis and transpiration. *Int. J. Remote Sens.*, **6,** 1335–1372.

——, 1987: Canopy reflectance, photosynthesis and transpiration. Part II: The role of biophysics in the linearity of their interdependence. *Remote Sens. Environ.*, **21,** 143–183.

——, and F. G. Hall, 1992: FIFE in 1992: Results, scientific gains, and future research directions. *J. Geophys. Res.*, **97,** 19 091–19 109.

——, and D. Schimel, 1993: Remote sensing of the land biosphere and biochemistry in the EOS era: Science priorities, methods

and implementation—EOS land biosphere and biogeochemical panels. *Global Planet. Change,* **7,** 279–297.

——, Y. Mintz, Y. C. Sud, and A. Dalcher, 1986: A simple biosphere model (SiB) for use with general circulation models. *J. Atmos. Sci.,* **43,** 505–531.

——, J. W. Shuttleworth, J. L. Dorman, A. Dalcher, and J. M. Roberts, 1989: Calibrating the simple biosphere model (SiB) for Amazonian tropical forest using field and remote sensing data. Part 1: Average calibration with field data. *J. Appl. Meteor.,* **28,** 727–759.

——, J. A. Berry, G. J. Collatz, C. B. Field, and F. G. Hall, 1992a: Canopy reflectance, photosynthesis and transpiration. Part III: A re-analysis using improved leaf models and a new canopy integration scheme. *Remote Sens. Environ.,* **42,** 187–216.

——, M. D. Heiser, and F. G. Hall, 1992b: Relations between surface conductance and spectral vegetation indices at intermediate (100 m^2 to 15 km^2) length scales. *J. Geophys. Res.,* **97,** 19 033–19 059.

——, S. O. Los, C. J. Tucker, C. O. Justice, D. A. Dazlich, G. J. Collatz, and D. A. Randall, 1994: A global 1° by 1° NDVI data set for climate studies. Part 2: The generation of global fields of terrestrial biophysical parameters from the NDVI. *Int. J. Remote Sens.,* **15,** 3519–3545.

——, D. A. Randall, G. J. Collatz, J. A. Berry, C. B. Field, D. A. Dazlich, C. Zhang, and L. Bounoua, 1996: A revised land surface parameterization (SiB2) for atmospheric GCMs. Part I: Model formulation. *J. Climate,* **9,** 676–705.

Singh, S. M., 1988: Simulation of solar zenith angle effect on global vegetation index (GVI) data. *Int. J. Remote Sens.,* **9,** 237–248.

Tarpley, J. D., S. R. Schneider, and R. L. Money, 1984: Global vegetation indices from the *NOAA-7* meteorological satellite. *J. Climate Appl. Meteor.,* **23,** 491–494.

Tucker, C. J., and M. Matson, 1985: Determination of volcanic dust deposition from El Chichón using ground and satellite data. *Int. J. Remote Sens.,* **6** (5), 619–627.

——, I. Y. Fung, C. D. Keeling, and R. H. Gammon, 1986: Relationship between atmospheric CO_2 variations and a satellite-derived vegetation index. *Nature,* **319** (6050), 195–199.

Vermote, E., N. El Saleous, Y. J. Kaufman, and E. Dutton, 1994: Data preprocessing: Stratospheric aerosol perturbing effect on the remote sensing of vegetation: Correction method for the composite NDVI after the Pinatubo eruption. *Société Internationale de Photogrammétrie et de Télédétection (ISPRS) Sixième Symp. Int.,* Val d'Isère, France, 151–158.

Zobler, L., 1986: A world soil file for global climate modeling. NASA Tech. Memo. 87802, NASA, Washington D.C. 35 pp.